Retrieved Vertical Profiles of Latent Heat Release Using TRMM Rainfall Products for February 1988

W.-K. TAO,[+] S. LANG,[+#] W. S. OLSON,[+@] R. MENEGHINI,[&] S. YANG,[+@] J. SIMPSON,[+] C. KUMMEROW,[+*] E. SMITH,[**] AND J. HALVERSON[+@]

[+]*Laboratory for Atmospheres, NASA Goddard Space Flight Center, Greenbelt, Maryland*
[#]*Science Systems and Applications, Inc., Lanham, Maryland*
[@]*Joint Center for Earth Systems Technology, University of Maryland, Baltimore County, Baltimore, Maryland*
[&]*Laboratory for Hydrospheric Processes, NASA Goddard Space Flight Center, Greenbelt, Maryland*
[**]*NASA Marshall Space Flight Center, Huntsville, Alabama*

(Manuscript received 8 March 2000, in final form 30 August 2000)

ABSTRACT

This paper represents the first attempt to use Tropical Rainfall Measuring Mission (TRMM) rainfall information to estimate the four-dimensional latent heating structure over the global Tropics for one month (February 1998). The mean latent heating profiles over six oceanic regions [Tropical Ocean and Global Atmosphere (TOGA) Coupled Ocean–Atmosphere Response Experiment (COARE) Intensive Flux Array (IFA), central Pacific, South Pacific Convergence Zone (SPCZ), east Pacific, Indian Ocean, and Atlantic Ocean] and three continental regions (South America, central Africa, and Australia) are estimated and studied. The heating profiles obtained from the results of diagnostic budget studies over a broad range of geographic locations are used to provide comparisons and indirect validation for the heating algorithm–estimated heating profiles. Three different latent heating algorithms, the Goddard Space Flight Center convective–stratiform heating (CSH), the Goddard profiling (GPROF) heating, and the hydrometeor heating (HH) algorithms are used and their results are intercompared. The horizontal distribution or patterns of latent heat release from the three different heating retrieval methods are very similar. They all can identify the areas of major convective activity [i.e., a well-defined Intertropical Convergence Zone (ITCZ) in the Pacific, a distinct SPCZ] in the global Tropics. The magnitudes of their estimated latent heating release are also in good agreement with each other and with those determined from diagnostic budget studies. However, the major difference among these three heating retrieval algorithms is the altitude of the maximum heating level. The CSH algorithm–estimated heating profiles only show one maximum heating level, and the level varies among convective activity from various geographic locations. These features are in good agreement with diagnostic budget studies. A broader maximum of heating, often with two embedded peaks, is generally derived from applications of the GPROF heating and HH algorithms, and the response of the heating profiles to convective activity is less pronounced. Also, GPROF and HH generally yield heating profiles with a maximum at somewhat lower altitudes than CSH. The impact of different TRMM Microwave Imager (TMI) and precipitation radar (PR) rainfall information on latent heating structures was also examined. The rainfall estimated from the PR is smaller than that estimated from the TMI in the Pacific (TOGA COARE IFA, central Pacific, SPCZ, and east Pacific) and Indian Oceans, causing weaker latent heat release in the CSH algorithm–estimated heating. In addition, the larger stratiform amounts derived from the PR over South America and Australia consequently lead to higher maximum heating levels. Sensitivity tests addressing the appropriate selection of latent heating profiles from the CSH lookup table were performed.

1. Introduction

The global hydrological cycle is central to climate system interactions and the key to understanding their behavior. Rainfall and its associated precipitation processes are a key link in the hydrologic cycle. Freshwater provided by tropical rainfall and its variability can exert a large impact upon the structure of the upper ocean layer. In addition, almost two-thirds of global rainfall occurs in the Tropics.[1] Precipitation from convective cloud systems makes up a large portion of tropical heating and rainfall. Furthermore, the vertical distribution of convective latent-heat release modulates large-scale tropical circulations [e.g., the 30–60-day intraseasonal oscillation; see Sui and Lau (1989)], which, in turn,

* Current affiliation: Department of Atmospheric Science, Colorado State University, Fort Collins, Colorado.

Corresponding author address: Dr. Wei-Kuo Tao, Mesoscale Atmospheric Processes Branch, Code 912, NASA/GSFC, Greenbelt, MD 20771.
E-mail: tao@agnes.gsfc.nasa.gov

[1] The Tropics is loosely defined as the longitudinal belt from 25°N to 25°S.

TABLE 1. Summary of previous latent heating algorithms and their applications.

Algorithm	Input	Cases	Resolution
Tao et al. (1991) HH algorithm	Surface rainfall, hydrometeor profiles (cloud water, rain, cloud ice, snow, and graupel), and terminal velocity of rain, snow, and graupel	GATE (1974), PRE-STORM (1985)	200–300 km daily
Tao et al. (1993a) CSH algorithm	surface rainfall and its stratiform percentage	GATE (1974), PRE-STORM (1985), Typhoon Thelma (1987)	200–300 km daily
Olson et al. (1999) GPROF heating algorithm	Cloud-modeled latent heating profiles and hydrometeor profiles	Hurricane Andrew (1992), TOGA COARE (1992–93)	25–50 km instantaneously
Yang and Smith (1999a,b) HH algorithm	Hydrometeor profiles (cloud water, rain, ice particles) and cloud vertical velocities/terminal velocity of rain and ice particles	TOGA COARE (1992–93) Global tropical region (1992)	15–50 km instantaneously 2.5° × 2.5° monthly
Tao et al. (1999) CSH algorithm	Surface rainfall and its stratiform percentage	TOGA COARE (1992–93)	500 × 500 km weekly

affect midlatitude weather through teleconnection patterns such as those associated with E1 Niño. Shifts in these global circulations can result in prolonged periods of droughts and floods, thereby exerting a tremendous impact upon the biosphere and human habitation. And yet, monthly rainfall over the tropical oceans was not known within a factor of 2 over large (5° latitude × 5° longitude) areas (Simpson et al. 1988, 1996). Hence the Tropical Rainfall Measuring Mission (TRMM), a joint U.S.–Japan space project, is an important mission. The TRMM science team selected a satellite observatory with an inclined low-altitude orbit and a combination of precipitation radar, visible–infrared, and microwave radiometers [see Simpson et al. (1996)]. TRMM, therefore, will provide a more accurate measurement of rainfall in addition to estimating the four-dimensional structure of latent heating over the global Tropics. The distributions of rainfall and inferred heating can be used to advance our understanding of the global energy and water cycle. In addition, this information can be used for global circulation and climate models for testing and improving their parameterizations.

Three types of latent heating profile retrievals have been developed for TRMM. The first algorithm estimates the latent heating profiles of clouds and cloud systems as a function of the vertical derivative of their retrieved hydrometeor profiles [termed a hydrometeor heating (HH) algorithm—see Tao et al. (1990) and Yang and Smith (1999a,b)]. The derivation and evaluation of the HH algorithm are based on cloud-resolving model (CRM) simulations and require information about the vertical profiles of cloud- and precipitation-sized water and ice particles, all of which can be obtained from the TRMM Microwave Imager (TMI) profile retrievals (Kummerow et al. 1996; Smith et al. 1992; 1994). The terminal (fall) velocities of the large cloud (precipitating) particles (rain, snow, and graupel/hail) are also required for the HH algorithm. Empirical coefficients associated with the condensation of small liquid water droplets and deposition of small ice particles are needed in Tao et al. (1990), and these coefficients can be determined using the surface rain rates (Tao et al. 1993a). Cloud-scale velocity is needed in Yang and Smith (1999b), and it is obtained by applying a regression method to a CRM-simulated database. The second method, the convective–stratiform heating (CSH) algorithm, only needs information on surface precipitation rates, amount of stratiform rain, and the type and location of observed cloud systems (Tao et al. 1993a). A lookup table, however, provides stored convective and stratiform latent heating profiles, normalized by surface rain rates, for various types of cloud systems in different geographic locations. These profiles are mostly obtained from CRM [Goddard Space Flight Center cumulus ensemble (GCE) model] simulations. In the third method, CRM-simulated hydrometeor/latent heating vertical profiles that have radiative characteristics consistent with a given set of multispectral microwave radiometric observations are composited to create (retrieve) a best estimate of the observed profiles [termed the Goddard profiling (GPROF) heating algorithm; Olson et al. (1999)]. Table 1 summarizes the cases and information needed in the previous latent heating retrieval studies.

Rainfall maps, stratiform amounts, and vertical structure of hydrometeors are generated on an operational basis from the TRMM retrieval algorithms. Products from TMI and from the precipitation radar (PR) can be used as input for the latent heating algorithms. The major objective of this study is to produce and to examine four-dimensional latent heating structures for February of 1998 using different TRMM rainfall products. In section 2, we will briefly review three different heating algorithms and their previous performance. The source of rainfall information derived from the TRMM sensors will be described in section 3. Retrieved latent heating profiles in global and in various geographic locations

will be examined and discussed in section 4. The CSH algorithm–retrieved latent heating structures will be compared with those produced by the GPROF algorithm and HH algorithm in section 5. A summary and future work will be presented in section 6.

2. TRMM heating algorithms

a. Hydrometeor heating algorithm

The HH algorithm, developed at The Florida State University, is based on the assumptions that an explicit three-dimensional cloud model can be used to provide the microphysical underpinnings for an inversion-based retrieval procedure, and that latent heating rates are proportional to the vertical derivatives of retrieved liquid–ice water mass fluxes. The algorithm is a fully physical inversion technique designed to accept any combination of polarized or unpolarized satellite or aircraft passive microwave measurements.

Yang and Smith (1999a) analyzed their retrieved latent heating profiles from Special Sensor Microwave Imager (SSM/I) and Q_2 (apparent moisture sink) profiles calculated from sounding data over the Tropical Ocean and Global Atmosphere Coupled Ocean–Atmosphere Response Experiment Intensive Flux Array (TOGA COARE IFA) area. They found that their latent heating profiles are generally in agreement with diagnosed Q_2 profiles, except that the retrieved latent heating has a secondary peak near 1 km. Yang and Smith (1999b) also retrieved time–space mean monthly latent heating from SSM/I for the 1992 annual cycle. The retrieved latent heating fields show many stationary and transient features that are consistent with studies concerning cloudiness, convection, and rainfall. However, the double-peak features of retrieved latent heating, a dominant peak near 5 km and a smaller one near 1 km, are not in good agreement with other diagnosed heating structures (e.g., Yanai et al. 1973; Thompson et al. 1979; Johnson 1984; Lin and Johnson 1996).

Yang and Smith (2000) modified their latent heating retrieval method by developing a new way to estimate a mean terminal velocity for liquid–ice water hydrometeors at SSM/I footprint scales. The small low-level peak in the latent heating profiles was eliminated in the new procedure. They compared the retrieved latent heating profiles and their diagnostic Q_1 (apparent heat source)–Q_2 structures for convective and stratiform conditions over the TOGA COARE IFA. Other published Q_1–Q_2 structures for similar conditions were also examined. Retrieved latent heating and diagnosed heating structures were similar for convective situations; however, lower tropospheric latent heating was not in agreement with diagnosed heating profiles. These results suggest that their latent heating retrieval method has difficulty separating convective and stratiform conditions.

b. Goddard profiling heating algorithm

Olson et al. (1999) retrieved atmospheric latent heating distributions associated with cloud systems that occurred during TOGA COARE and Hurricane Andrew (1992) using SSM/I observations. Their estimation of the latent heating in Hurricane Andrew showed an increase in upper-level heating (near the inner core) as Andrew intensified. No (direct or indirect) observational data were available for validation in Andrew. However, the diagnosed relationship between latent heating and intensification has been noted in previous studies—see Rodgers et al. (1994). Olson et al.'s (1999) retrieved latent heating profiles for the TOGA COARE IFA show a low bias in the altitude of the maximum heating as well as excessive low-level cooling when compared with rawinsonde-derived profiles.

The method of Olson et al. (1999) has been modified and adapted to observations of TMI. First, the method of Hong et al. (1999) for estimating the fractional coverage of convection within a footprint from TMI brightness temperature horizontal texture has been combined with a new method for inferring the convective fraction from TMI 85.5-GHz polarization data. This combined estimate of convective area fraction within a TMI footprint weighs the texture- and polarization-based estimates using the expected error variance of each estimate. When radiative scattering is weak, the texture-based method has the greatest influence on the combined estimate, whereas in regions of strong radiative scattering the polarization-based method prevails.

This combined estimate of convective fraction is used to constrain TMI-retrieved latent heating profiles from GPROF—see section 3a. As shown by Olson et al. (1999), the estimated convective fraction has a significant impact on estimates of the latent heating profile, since convective and stratiform regions are associated with fairly distinct vertical heating structures.

c. Convective–stratiform heating algorithm

Diagnostic budget studies (Houze 1982; Johnson 1984) have shown that the distribution of heating in the anvil region of tropical mesoscale cloud systems is considerably different from the vertical profile of heating in the convective region. Tao and Simpson (1989), McCumber et al. (1991), and Tao et al. (1991; 1993b) have also shown that the microphysical processes are very different in the convective and stratiform regions for GCE model–simulated GATE, TAMEX, EMEX, and PRE-STORM mesoscale convective systems.[2] For example, evaporative cooling in the lower troposphere is dominant in the stratiform region in all simulated con-

[2] GATE stands for Global Atmospheric Research Program Atlantic Tropical Experiment, TAMEX for Taiwan-Area Mesoscale Experiment, EMEX for Equatorial Mesoscale Experiment, and PRE-STORM for Preliminary Regional Experimental for Storm Central.

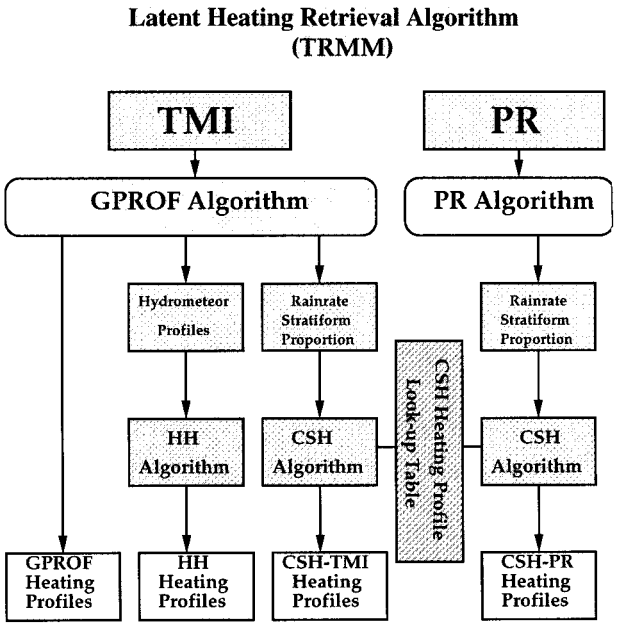

FIG. 1. Diagram showing the procedure for deriving a latent heating profile using the CSH, HH, and GPROF heating algorithms. Various rainfall products needed for these three different heating algorithms are shown. The heating profiles in the lookup table are from diagnostic and CRM-simulated convective and stratiform heating profiles for various geographic locations.

vective systems. On the other hand, condensational/depositional heating is dominant in the convective region of these systems. Based on these findings, a convective–stratiform heating algorithm has been developed (Tao et al. 1993a). Figure 1 is a flow chart that shows the procedure for deriving a latent heating profile from the CSH algorithm and the HH and GPROF heating algorithms. There are many sets of normalized heating profiles; each set has a convective profile and a stratiform profile simulated by a cloud-resolving model (or cumulus ensemble model) or estimated from a diagnostic budget study. Each set represents different system organizations as well as various geographic locations. The CSH-derived heating profile can be evaluated by comparing it with those estimated from well-designed field campaigns [i.e., GATE, TOGA COARE, Australian Monsoon Experiment (AMEX), Amazon Boundary Layer Experiment (ABLE), and TRMM field programs]. Inputs for the CSH algorithm are from spaceborne (TMI, PR, and SSM/I) algorithm derivations.

Vertical profiles of latent heat release and their retrieval using the CSH algorithm from three TOGA COARE convectively active periods[3] were examined by Tao et al. (2000). The inputs for the CSH algorithm are SSM/I-(similar to TMI) and ship-based radar (similar to TRMM PR)–derived rainfall and stratiform amount. The 2D GCE model–simulated surface rainfall and stratiform amount were also used to assess the strengths and/or deficiencies of the CSH algorithm. The GCE model–simulated rainfall, stratiform amount, and latent heating profiles were in excellent agreement with those estimated by upper-level soundings and large-scale analyses (Lin and Johnson 1996). In addition, the typical convective and stratiform heating structures (Johnson 1984; Houze 1989, 1997) were well captured by the GCE model. In the current study, these modeled convective and stratiform heating profiles are used to expand the set of heating profiles in the CSH algorithm's lookup table.

Temporal variability of CSH algorithm–retrieved latent heating profiles using radar-estimated rainfall and stratiform amount was in good agreement with that diagnostically determined for all three periods. However, less rainfall and a smaller stratiform percentage estimated by ship-based radar[4] resulted in weaker (underestimated) latent heating profiles and lower maximum latent heating levels when compared with those determined diagnostically. Rainfall information from SSM/I could not be used to retrieve individual convective events because of poor temporal sampling. The altitude of maximum latent heating from the SSM/I-derived time-averaged stratiform amount was lower than that diagnostically determined for 19–27 December 1992. Tao et al. (2000) performed a sensitivity test by adding 10% to the SSM/I stratiform amount. The altitude of maximum latent heating resulting from this adjustment was in very good agreement with that diagnostically determined (Lin and Johnson 1996). It may be inferred that the SSM/I-derived time-averaged stratiform amount was originally underestimated for 19–27 December. A higher (lower) percentage of stratiform rain can imply a maximum heating rate at a higher (lower) altitude (Tao et al. 1993b). Time-averaged heating profiles derived from SSM/I, however, were in reasonable agreement with those derived from soundings for the 10–17 December and 9–13 February convective periods. The heating retrievals may be more accurate for longer timescales provided there is no bias in the sampling.

3. TRMM rainfall products

Daily 0.5°-gridded rainfall and percentage of rainfall classified as convective from TMI and PR for February of 1998 are produced using GPROF (Olson et al. 1999) and the TRMM PR algorithms (Awaka et al. 1998; Iguchi et al. 2000; Meneghini et al. 2000), respectively. This fine-resolution rainfall product will be used as the

[3] Three episodes (11–17 December 1992, 19–27 December 1992, and 9–13 February 1993) containing intense convection associated with westerly wind bursts and super cloud clusters that occurred over the IFA were studied.

[4] Johnson and Ciesielski (2000) indicated that the ship radars were located within a relatively dry region of the IFA. The smaller rainfall estimated from the ship radars could also be caused by the specific radar reflectivity–rainfall rate (Z–R) relationship applied in the stratiform region by Short et al. (1997).

input for the CSH algorithm. Note also that the HH algorithm developed by Yang and Smith (1999a,b, 2000) will use the input from the Goddard profiling algorithm (Olson et al. 1996) in this study.

a. Goddard profiling algorithm

The basis of GPROF is the estimated expected value or ''Bayesian'' technique originally described in Kummerow et al. (1996) and Olson et al. (1996). A detailed description of the retrieval method utilized in the current study, including direct latent heating estimation, may be found in Olson et al. (1999).

In GPROF, TMI-observed radiances in the different sensor channels are compared with corresponding simulated radiances based upon a variety of cloud-resolving model–generated cloud and precipitation fields. Retrieved precipitation and heating profiles are constructed from those model-generated profiles that are radiatively consistent with the observations. The varying resolution of the different microwave channels is included in the simulated radiances by calculating the upwelling radiance field at model resolution ($\sim$1 km) and then convolving the field by the appropriate sensor antenna pattern for a particular channel. In current applications of the TMI retrieval method, surface rainfall rate is defined as the 10 km $\times$ 10 km area-average rain rate at the lowest model level. The dimension of the averaging area (10 km) corresponds to the resolution of the 37-GHz TMI channel. Convective rain fraction is defined by first classifying each model grid point as either convective or nonconvective using the technique described in Tao et al. (1993b) and then applying

$$f_R \equiv \frac{\sum_{i,j} R_{ij}\delta_{ij}}{\sum_{i,j} R_{ij}}, \tag{1}$$

where

$$\delta_{ij} \equiv \begin{cases} 0 & \text{nonconvective grid point} \\ 1 & \text{convective grid point.} \end{cases} \tag{2}$$

Here, R_{ij} is the rain rate associated with grid point ij, and the summation is over all grid points within a given 10 km $\times$ 10 km area.

Vertical precipitation and latent heating profiles are similarly determined by averaging the individual grid-point model-derived profiles over 10 km $\times$ 10 km areas—see Olson et al. (1999) for more details. In this study, the 10 km $\times$ 10 km average surface rain rate, convective rain fraction, precipitation profiles, and latent heating profile are all retrieved from TMI observations using the GPROF algorithm.

b. TRMM PR rainfall algorithm

The TRMM PR operates at a frequency of 13.8 GHz. This is a moderately attenuating frequency, so one of the major objectives of the PR algorithms is to estimate and to correct for the path attenuation. Because the PR is a single-wavelength, single-polarization, non-Doppler radar, there are only a few methods available. These include the Hitschfeld–Bordan (HB) method (Hitschfeld and Bordan 1954), the surface reference technique or SRT (Meneghini et al. 1983), a ''hybrid'' of these (Iguchi and Meneghini 1994; Iguchi et al. 1998), and the mirror-image technique (Liao et al. 1999). The rain-rate estimation algorithm (which in the TRMM nomenclature is called 2a25) uses a hybrid of the HB method and SRT to correct for attenuation and to derive an estimate of the range profile of the radar reflectivity factor Z (dBZ). The rain-rate R profile is then calculated from the Z profile and an appropriate Z–R relationship. The algorithm also includes surface clutter rejection and an attempt to correct for effects of nonuniform beamfilling.

The major sources of data to the algorithm are the measured radar reflectivity factors (dBZ_m) derived from the radar return power without attenuation correction, and an estimate of path attenuation via the surface reference technique (algorithm 2a21) with an associated reliability or accuracy of this estimate. The algorithm first defines the processing region, using only the data between the rain top and the lowest height above the surface that is free from surface clutter. The brightband height and the climatological freezing height are used to define the regions of liquid, solid, and mixed-phase hydrometeors. The initial values of the k (attenuation coefficient)–Z and Z–R relations are defined accordingly.

Hitschfeld and Bordan (1954) showed that attenuation correction from a single attenuating wavelength can be accomplished if a k–Z relationship is used. By differentiating the radar equation with respect to range, a first-order differential equation is obtained, the solution of which provides the attenuation-corrected Z and rain rate. The authors point out that the solution tends to become unstable with increasing attenuation, so an error in the radar constant or in the k–Z relationship can lead to unrealistic rain-rate estimates.

The attenuation correction is based primarily on SRT, which assumes that the decrease in the apparent surface cross section is caused by the propagation loss in rain. The coefficient α in the $k = \alpha Z^b$ relationship [where k is the attenuation coefficient (dB km^{-1})] is adjusted so that the path-integrated attenuation (PIA), estimated from the HB method, matches that obtained from SRT. This ''α-adjustment'' method assumes that the discrepancy between the PIA estimates from SRT and HB can be attributed to an inappropriate choice of α or, equivalently, an inappropriate choice of the raindrop size distribution. There are other ways, however, to use the path attenuation information provided by SRT either by adjusting the radar constant (Meneghini et al. 1983) or by using the SRT path attenuation as a final value in the solution to be HB equation (Amayenc et al. 1996).

To avoid inaccuracies in the attenuation correction

when SRT is unreliable, a hybrid of the SRT and the HB method is used (Iguchi and Meneghini 1994; Iguchi et al. 1998). Generally, when the rain rate is low, the path attenuation determined from the HB method is weighted more heavily than SRT, which tends to have a large relative error at these rain rates. When the rain rate is moderate or high, the SRT estimate of path attenuation is normally given more weight than the HB method, thereby avoiding the instabilities that usually occur in the HB estimate when the path attenuation is large.

Convective–stratiform classification of the rain is based on a combination of the vertical and horizontal structure of the radar reflectivity field (Awaka et al. 1998). The vertical profile is checked for the presence of a bright band (melting layer) by considering the behavior of the second derivative of the radar range profile. Unless the maximum dBZ exceeds a threshold, the presence of a well-defined bright band is used to indicate stratiform rain. In cases in which a clearly defined melting layer is absent, the horizontal rain structure is examined by means of a modified version of an algorithm designed for the analysis of ground-based radar data (Steiner et al. 1995).

Statistics of the instantaneous, high-resolution rain rates are compiled on a monthly basis over $5^\circ \times 5^\circ$ latitude–longitude grids. Near-surface rain rates and the rain rates at five altitude levels are stored according to rain type. The statistics include means, standard deviations, and histograms of the rain rate, radar reflectivity factors, bright band, and storm heights.

4. Results

Verification of the retrieved global and regional latent heating profiles is not an easy task because of the lack of direct observations both temporally and spatially on the global and regional scales. The heating profiles obtained from the results of diagnostic studies over a broad range of geographic locations as well as different years (e.g., Yanai et al. 1973; Chen 1980; Johnson 1984, 1992; Frank and McBride 1989; Houze 1989; Greco et al. 1994; Lin and Johnson 1996) will be used to provide comparisons and indirect validation for this study.

a. Rainfall and stratiform amount

Figures 2a,b show the monthly mean surface rainfall (mm day^{-1}) for February of 1998 derived from TMI (GPROF) and PR, respectively. Rainfall characteristics and latent heating structures over the six oceanic regions (TOGA COARE IFA, central Pacific, South Pacific Convergence Zone, east Pacific, Indian Ocean, and Atlantic Ocean) and three continental regions (South America, central Africa, and Australia) shown in Fig. 2a will be examined and compared. Clearly, a well-defined ITCZ (associated with heavy precipitation) is present in the central Pacific between the equator and 5°S. The ITCZ is located between 5°N and 5°S over the east Pacific. Weak convective episodes are present over the South Pacific Convergence Zone (SPCZ). Note that heavy precipitation is not located in the TOGA COARE IFA region. A similar situation was found during TOGA COARE (December 1992–February 1993). Over the Indian Ocean, the precipitation events extend from southwest to northeast. Over the Atlantic Ocean, a more distinct ITCZ is present over the west Atlantic than over the east Atlantic. The precipitation episodes (monthly) over the continental regions are somewhat different from those over oceans. Heavy precipitation over Africa and Australia is centered, respectively, at 10°S and between 20°N and 15°S. Over South America, heavy precipitation events are spread over a relatively large area. PR-derived monthly precipitation patterns are also similar to that of GPROF except for the region near 35°N in the Pacific Ocean and in the Atlantic Ocean (Fig. 2b).[5] Both TMI and PR rainfall products will be used in the CSH algorithm.

TABLE 2. The TMI GPROF– and PR algorithm–derived rainfall and stratiform percentage for Feb of 1998 for the various geographic locations identified in Fig. 2. Entries are of the form GPROF/PR.

	Avg rainfall (mm day^{-1})	Mean stratiform (%)
TOGA COARE IFA region	4.72/3.44	45/50
Central Pacific	11.64/7.07	54/61
East Pacific	7.75/4.16	52/58
South Pacific Convergence Zone	2.58/1.84	57/59
Indian Ocean	4.27/3.26	51/50
Atlantic Ocean	1.13/1.12	39/31
South America	4.79/4.14	25/44
Africa	1.85/1.59	24/32
Australia	2.20/1.92	30/49

Several aspects of the rainfall distributions shown in Fig. 2 are broadly consistent with an anomalous distribution of rainfall due to a strong, active El Niño event during the boreal winter of 1998 (S. Curtis 2000, personal communication). A global map of ENSO precipitation anomaly for February 1998 generated using the Global Precipitation Climatology Project (Huffman 1997), a technique that estimates global rainfall from a combination of the Geostationary Operational Environmental Satellite infrared and Defense Meteorological Satellite Program SSM/I datasets, exhibits the following features: 1) positive rainfall anomalies exceeding 5–6 mm day^{-1} in the central and eastern Pacific and also the winter monsoon trough region of the Southern Hemisphere Indian Ocean; 2) a pronounced negative

[5] Examination of rainfall distributions and comparisons between PR and GPROF are the current focus of the TMI and PR algorithm developers. Varying the drop size distributions as well as explicit modeling of melting in the cloud-resolving model simulations supporting the GPROF algorithm could lead to a significant change in the estimated surface rain and its stratiform percentage. The Goddard cloud modeling and rainfall retrieval groups are working closely to resolve this issue.

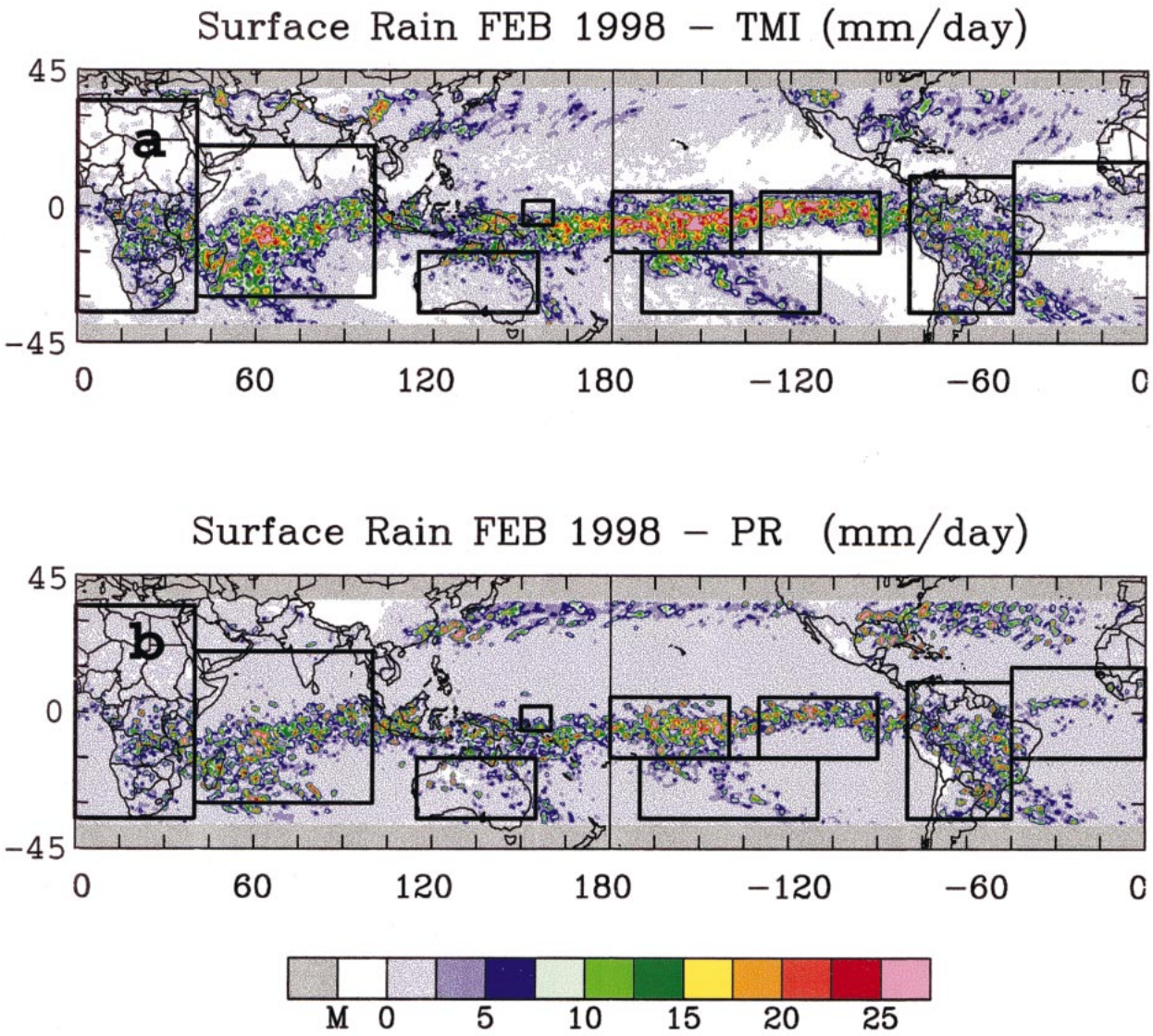

FIG. 2. Monthly mean rainfall (mm day^{-1}) for Feb of 1998 derived by (a) GPROF and (b) PR. The rainfall and its stratiform amount as well as the latent heating profiles will be compared and examined for the various geographic locations identified by the boxes.

anomaly encompassing much of the western Pacific warm pool region, with a maximum rainfall deficit of -8 mm day^{-1} centered in the IFA region; and 3) reduced rainfall amounts (-4 to -5 mm day^{-1}) extending across the entire Atlantic ITCZ region and into northeastern Brazil. These patterns of rainfall excess and deficit are classic ''signatures'' of a strong El Niño teleconnection pattern and qualitatively explain much of the global variation observed in the independently measured amounts based on the GPROF technique.

Table 2 shows the TMI (GPROF)- and PR algorithm-derived rainfall and its stratiform percentage for nine (six over the tropical oceans and three over land) different geographic locations. Overall, PR-derived rainfall is smaller than rainfall estimated by TMI for all nine geographic locations, especially over the central and east Pacific Ocean (40% and 23% difference, respectively). Rainfall from the TMI and PR over the Atlantic Ocean is almost identical (less than a 1% difference). The difference between TMI and PR rainfall estimates is smaller over continental regions (where it is less than 14%) than over the Pacific and Indian Oceans. Note that both sensors indicate the heaviest rainfall over the central Pacific and the weakest over the Atlantic Ocean.

Stratiform rain amounts are estimated to be about 40%–50% in organized convective systems in the Tropics (Houze 1997), with lower stratiform amounts (~30%–40%) in continental convective systems (Rutledge and Houze 1987; Johnson and Hamilton 1988). Therefore, both TMI- and PR-estimated stratiform percentages associated with oceanic and continental convective systems are reasonable. The results from Table

2 also indicate that the difference between TMI- and PR-estimated stratiform percentage over the oceans is smaller than that over land. Small differences (5%–7%) in the stratiform percentage from tropical oceanic convection ensure the retrieval of similar levels (altitudes) of maximum latent heating (Tao et al. 1993a). The difference in stratiform percentage over South America and Australia is large (19%). Note that stratiform percentages are lower over the Atlantic, South America, and Africa relative to the Pacific and Indian Oceans from both the TMI (GPROF) and PR algorithms.[6]

b. Latent heating profiles in the CSH lookup table

Selecting the appropriate latent heating profiles from the CSH algorithm's lookup table for specific convective events is not a trivial problem. Of course, the best set of heating distributions would be based on numerical simulations or diagnostics (using upper-air soundings during intensive field campaigns) of one or more ''representative'' events observed during the period of interest. Initial conditions required for the cloud-resolving model simulations are accurate vertical distributions of temperature, water vapor, and winds and can only be obtained from field campaigns. It is very expensive to conduct field campaigns (with a dense upper-air sounding network) over various geographic locations and at different seasons, however.

Two different approaches for selecting the latent heating profiles in the lookup table are used to obtain distinct estimates of the latent heating profiles in this study. In the first approach, normalized heating profiles representing oceanic and continental regions (Figs. 4a,b) are obtained by averaging profiles from the lookup table based on a set of diagnostic studies (Fig. 3) and the growing (but still limited) number of GCE model simulations (Figs. 4c–h). The diagnostically determined profiles are from Gallus and Johnson (1991; PRE-STORM), Yanai et al. [1973; partitioned into convective and stratiform components by Johnson (1984); Marshall Islands], Houze (1989; GATE), Houze and Rappaport (1984; GATE) and Chong and Hauser (1990; Africa). The model-simulated profiles are from Tao and Simpson (1989; GATE), Tao et al. (1991; TAMEX, not shown), Tao et al. (1993b; EMEX and PRE-STORM) and Tao et al. (2000; west Pacific warm pool region). In the second approach, the heating profiles from lookup table profiles based on geographic locations and months of interest [i.e., Pacific (including TOGA COARE 10–17 and 19–27 December 1992 and 9–13 February 1993), Atlantic, Africa, North America, and TOGA COARE from February of 1993] are utilized in the CSH algorithm.

The heating profiles (normalized by surface rain rate) shown in Fig. 4 have characteristic shapes corresponding to convective and stratiform regions (e.g., Houze 1982, 1997). These regions include maximum convective heating in the lower to middle troposphere, maximum stratiform (anvil) heating in the upper troposphere, and regions of stratiform cooling prevailing in the lower troposphere. Also, larger heating aloft in the stratiform region is associated with larger cooling in the lower troposphere. However, some notable differences do exist. First, convective heating is much weaker than the associated stratiform heating aloft in continental convective systems (Fig. 4b). On the other hand, the con-

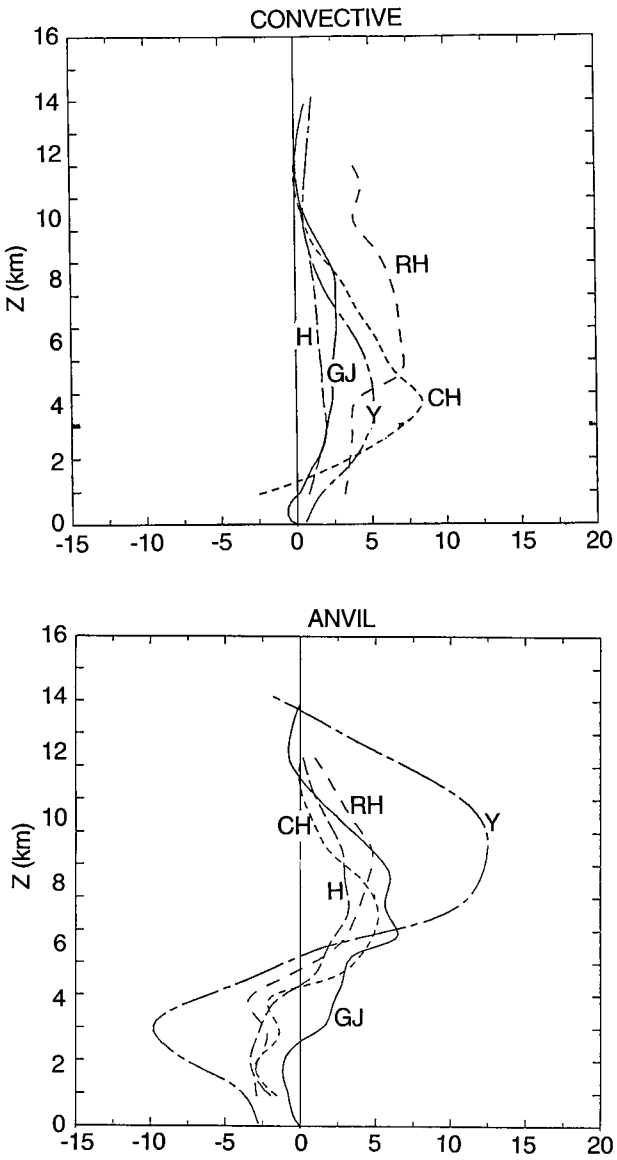

FIG. 3. Comparison of vertical Q_1 profiles normalized by rainfall rates for averages taken (top) over the convective region and (bottom) over the stratiform region. These profiles are from Gallus and Johnson (1991; curve GJ), Yanai et al. [1973; partitioned into convective and stratiform components by Johnson (1984); curve Y], Houze (1989; curve H), Houze and Rappaport (1984; curve HR), and Chong and Hauser (1990; curve CH). Units: $(^\circ\ \text{day}^{-1})\ (\text{cm day}^{-1})^{-1}$.

[6] An effort to determine whether PR overestimates or TMI underestimates the stratiform rain amount will be part of a future investigation.

vective heating is as strong as the stratiform heating for the oceanic convective systems (Fig. 4a). Warm-rain processes and stratiform rain are more prevalent in tropical oceanic convective systems than in continental systems, which may be the reason for these differences in latent heating. Second, the level separating the heating and cooling in the stratiform region is higher in the oceanic convective systems than in the continental systems. The differences in the depth of the stratiform region cooling probably reflect differences in melting-layer height for contrasting tropical oceanic, continental, and midlatitude airmass source regions. Third, the heating and cooling associated with the stratiform region for convective episodes that occurred during 9–13 February 1993 (Fig. 4e) are stronger than during 10–17 and 19–27 December 1992 (components of Fig. 4c). This feature may be explained by the fact that the convective systems that occurred during February 1993 had more stratiform clouds than those from the December periods (Lin and Johnson 1996; Tao et al. 2000). In addition, stratiform cooling in the Atlantic (GATE), Australia, and Africa profiles is relatively small. The cooling is very strong near the surface in the African convective system because of a dry boundary layer (Caniaux et al. 1994). The latent heating profiles modeled by the GCE and determined kinematically[7] are very different in the GATE convective system. The impact of the lookup-table profiles on the retrieved latent heating profiles will be assessed in the next section.

c. *Gridded 0.5° × 0.5° daily and monthly latent heating profiles*

1) HORIZONTAL DISTRIBUTION OF LATENT HEAT RELEASE

Figure 5 shows monthly mean latent heating at three different altitudes (2, 5, and 8 km) over the global Tropics from the CSH algorithm using TMI-derived rainfall products and latent heating profiles in the lookup table representing general tropical oceanic and land regions (the first approach). The horizontal pattern of CSH-estimated latent heating structures is very similar to the pattern of surface rainfall (Fig. 2), especially at middle and upper levels. For example, a well-defined ITCZ in the east and central Pacific and in the Atlantic Ocean, a distinct SPCZ, and broad areas of precipitation events spread over the continental regions are present. Also, stronger latent heat release (10 K day^{-1} or greater) in the middle and upper troposphere is always associated with heavier surface precipitation. Heating in the upper troposphere over the Pacific and Indian Oceans is much stronger than the heating over Africa, South America, and the Atlantic Ocean. A higher tropopause and warmer surface temperatures over the Pacific may be the reason for the higher level of maximum latent heating. Differential heating between land and ocean in the upper troposphere could generate strong horizontal gradients in the thermodynamic fields and interact with the global circulation.

One interesting result from Fig. 5 is the relatively strong cooling (-1 to -2 K day^{-1}) at the 2-km level over the (east, central, and south) Pacific and Indian Oceans but not over the continental regions (i.e., Africa and South America). This result is due to the fact that the TMI observations had less stratiform precipitation over the continental regions (see Table 2), which is not conducive to retrieving stronger low-level cooling over the continental regions relative to the tropical oceans. However, it is still not an expected result, because the moisture content is higher over oceans. Cooling by evaporation of raindrops in the lower troposphere should be stronger over dry areas. Several previous observational studies were performed to analyze the heating budget obtained from sounding networks over the Pacific warm pool region and the Amazon region. For example, Lin and Johnson (1996) found weak cooling at low levels, probably induced by mesoscale downdrafts or evaporation by shallow cumuli, in the mean heating profile over the TOGA COARE region for the month of February 1993. Greco et al. (1994) calculated latent heating profiles from the ABLE network. Their results indicated that the distribution of heating is very similar to that of West African squall lines (Chong and Hauser 1990). Peak heating occurs between 500 and 550 hPa (about 5–6 km). Their results did not exhibit low-level diabatic cooling for the ABLE case. They suggested that the lowermost 2–3 km over the Amazon rain forest canopy is characterized by a strong diurnal cycle of evapotranspiration and upward convective fluxes of moisture producing very large mixing ratios (Fitzjarrald et al. 1990). Model results (Scala et al. 1990) also suggested that dry tropospheric air is not present for the production and maintenance of evaporatively cooled downdrafts. The high moisture content during the wet season in the lower troposphere of the Amazon Basin may prevent or severely limit cooling below cloud base. Thus, more low-level cooling over the Pacific than over South America as estimated by the CSH heating algorithm is, perhaps, reasonable.

The CSH algorithm–estimated latent heating distributions from the second approach (selecting the heating profiles from the lookup table based on geographic location and month of interest) is shown in Fig. 6. In this case, the latent heating profiles shown in Figs. 4a,c–h are utilized.[8] The horizontal distributions and variations of latent heating structures (i.e., Pacific and Atlantic

[7] The convective and stratiform heating profiles were derived using composite ''kinematic and thermodynamic'' fields from radar, upper-air soundings, and aircraft-measured winds.

[8] The profiles shown in Fig. 4d were selected for the Atlantic region; Fig. 4e for the central Pacific, east Pacific, and TOGA COARE IFA regions; Fig. 4f for Africa; Fig. 4g for South America; Fig. 4h for Australia; and Fig. 4a for all other oceanic regions.

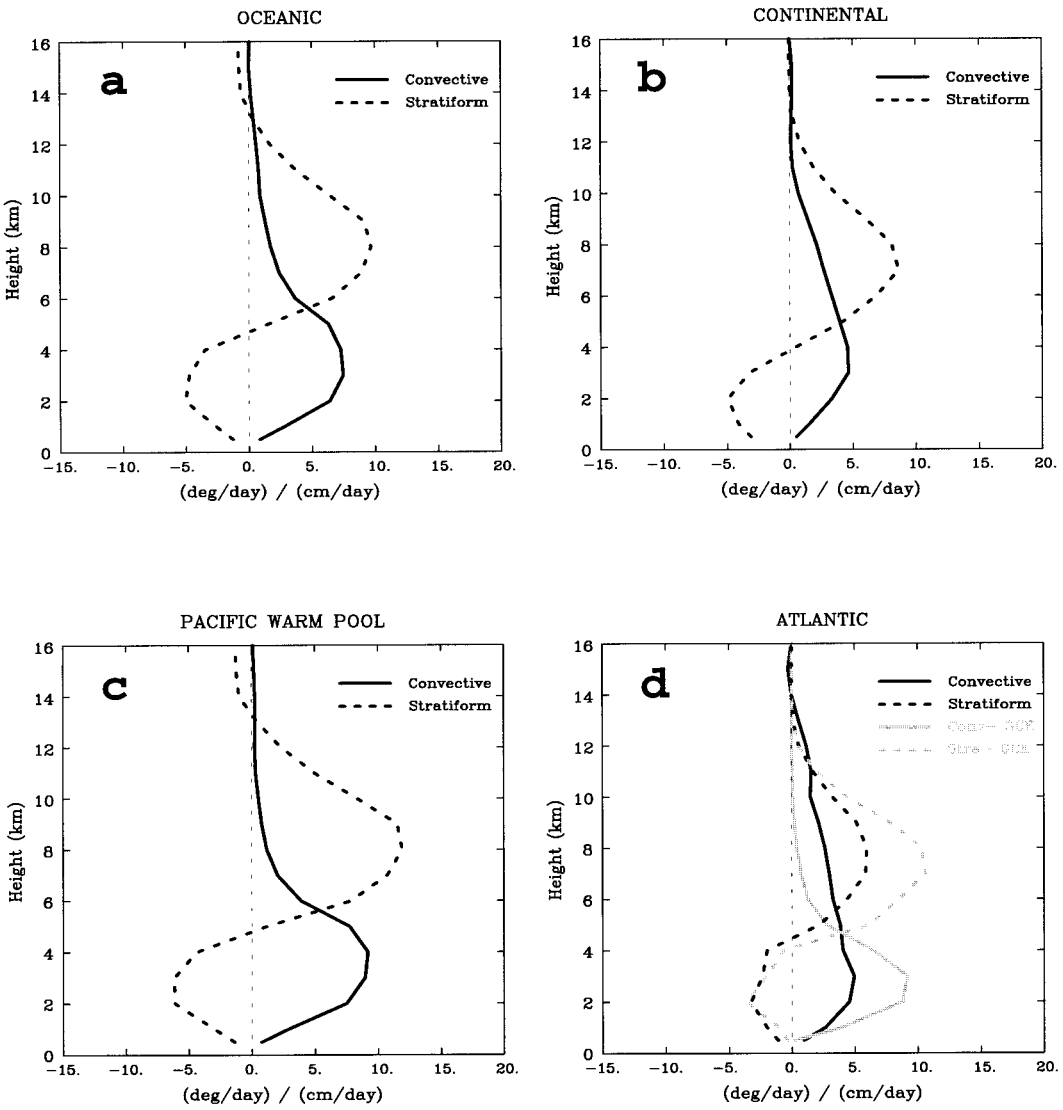

FIG. 4. The convective and stratiform heating profiles stored in the heating profile lookup table for the CSH algorithm. The profiles represent (a) tropical oceans, (b) general land areas, (c) the Pacific warm pool region, (d) the east Atlantic region (GATE, both total averaged and GCE simulated), (e) the TOGA COARE IFA for Feb of 1993, (f) Africa (Convection Profonde Tropicale: COPT-81), (g) midlatitude United States (PRE-STORM), and (h) Australia (EMEX). Units: ($^\circ$ day^{-1}) (cm day^{-1})$^{-1}$.

ITCZ, an SPCZ, and relatively scattered organization in Africa and South America) in Figs. 5 and 6 are very similar. Areas of cooling over the Pacific and Indian Oceans and heating over the continental regions at low levels are also present in the retrieved latent heating structures using the second approach. However, there are some notable differences between Figs. 5 and 6. The latent heat release at the 2-km level is stronger and extends over a larger area in the South American and Australian regions based upon the second approach. In addition, the latent heat release at middle and upper levels is stronger over the TOGA COARE IFA and central and east Pacific regions than the heating based on general oceanic and continental heating profiles from the CSH lookup table. These results are simply explained by the fact that the heating profiles selected for use in the CSH lookup table are very different in the two approaches. For example, the central and east Pacific latent heating profiles shown in Fig. 4e are utilized in the second approach, and these profiles exhibit greater heating/cooling maxima than do the oceanic heating profiles utilized in the first approach—see Fig. 4a.

2) MONTHLY MEAN LATENT HEATING PROFILES OVER VARIOUS GEOGRAPHIC LOCATIONS

Figure 7 shows the monthly (February 1998) mean latent heating profiles derived from the CSH heating

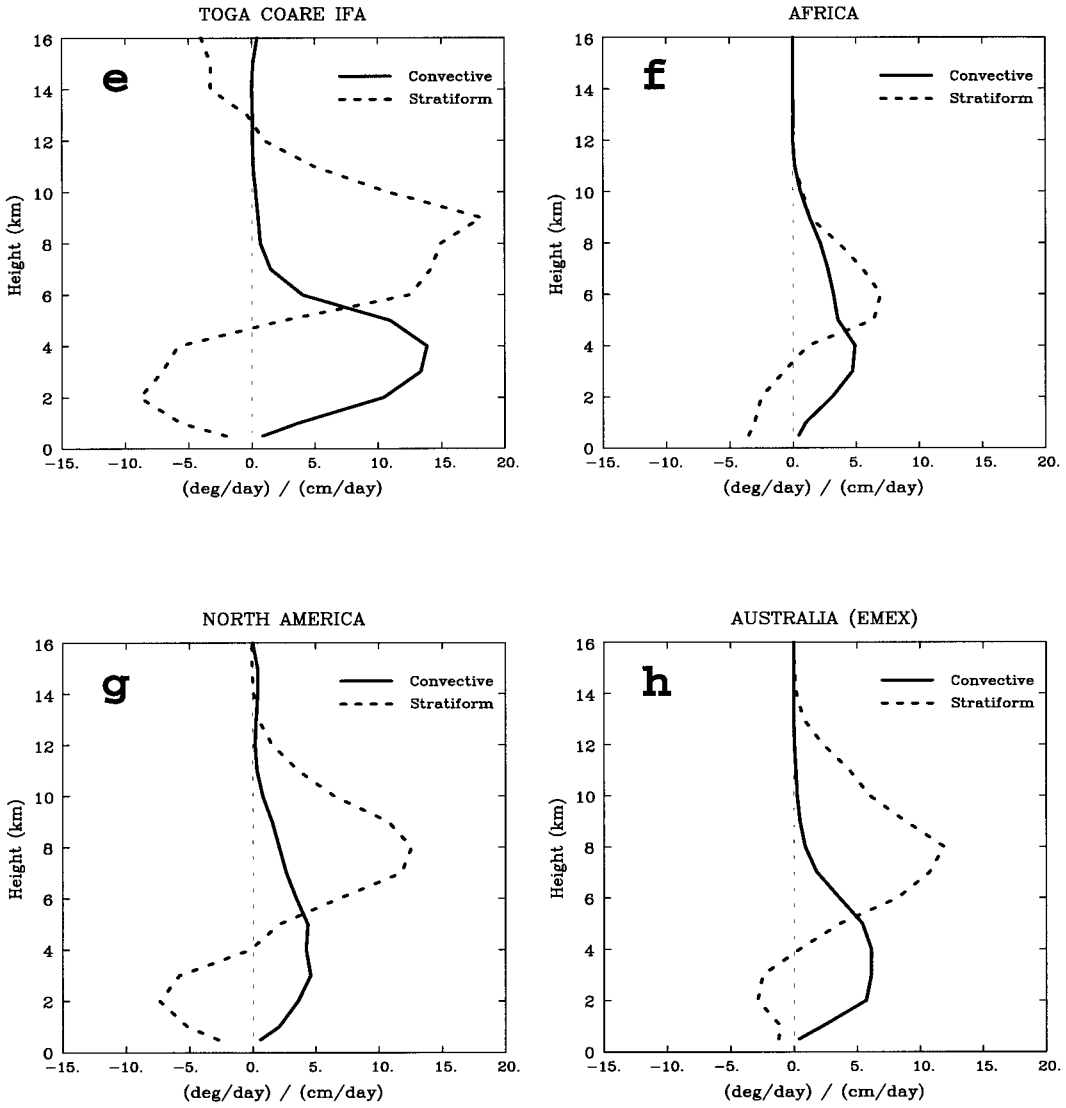

FIG. 4. (*Continued*)

algorithm for various geographic locations. Both approaches for selecting the heating profiles from the look-up table (Figs. 5 and 6) are shown. Over the central and east Pacific regions, the latent heating profiles are very similar in terms of the maximum heating level (near 8 km) and low-level cooling (about 1° day^{-1}). Over the TOGA COARE IFA region, the cooling at low levels is smaller than in the central and east Pacific regions. This result is caused by a smaller stratiform amount (45%) over the TOGA COARE IFA as compared with the central and east Pacific (52%–54%). Over the SPCZ, the heating/cooling below 3 km is very weak, but there is much stronger heating aloft. Over tropical continental regions, the low-level cooling is present as it is over the Pacific, but it is very weak (less than 0.2° day^{-1}). In addition, the altitude of maximum heating over Africa, South America, and the Atlantic Ocean is lower than that over the Pacific and Indian Oceans. A higher altitude of maximum heating over the Pacific and Indian Oceans relative to Africa, South America, and the Atlantic Ocean is in good agreement with diagnostic budget studies. The higher tropopause and warmer surface temperatures over the tropical oceans as suggested by Thompson et al. (1979) and Johnson (1992) could be the reasons for the higher altitude of maximum latent heating over the Pacific as compared with the Atlantic and Australia. The difference in retrieved convective and stratiform proportion among the various geographic locations could also account for the difference in the heights of the maximum latent heating. Higher stratiform amounts always contribute to higher altitudes of maximum latent heating. Whether the higher stratiform proportions or more frequent vigorous convective events in the Pacific are associated with higher SSTs

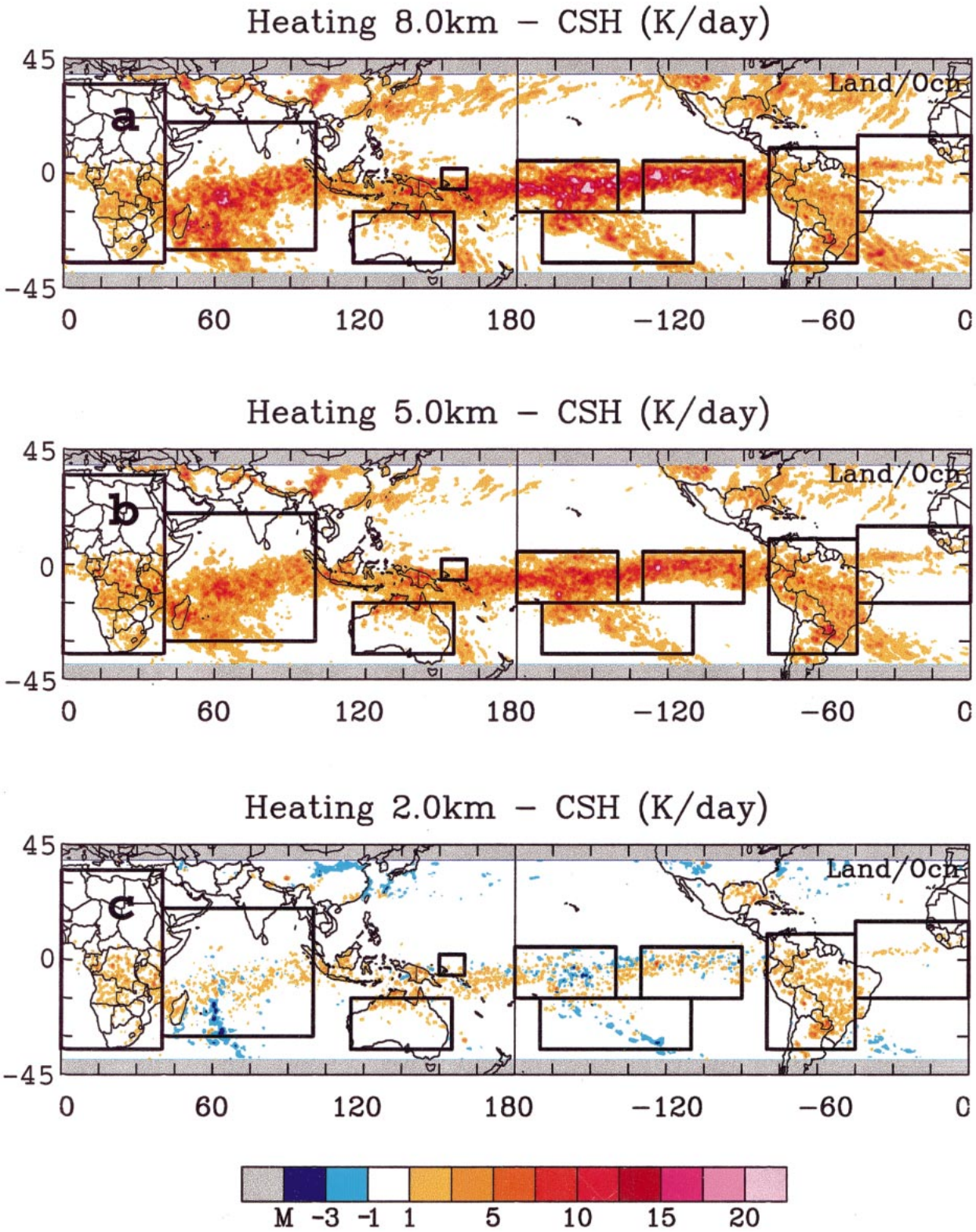

FIG. 5. Monthly mean latent heating profiles at (a) 8, (b) 5, and (c) 2 km above ground level over the global Tropics. Latent heating profiles representing just tropical oceanic and general land regions from the CSH lookup table were used.

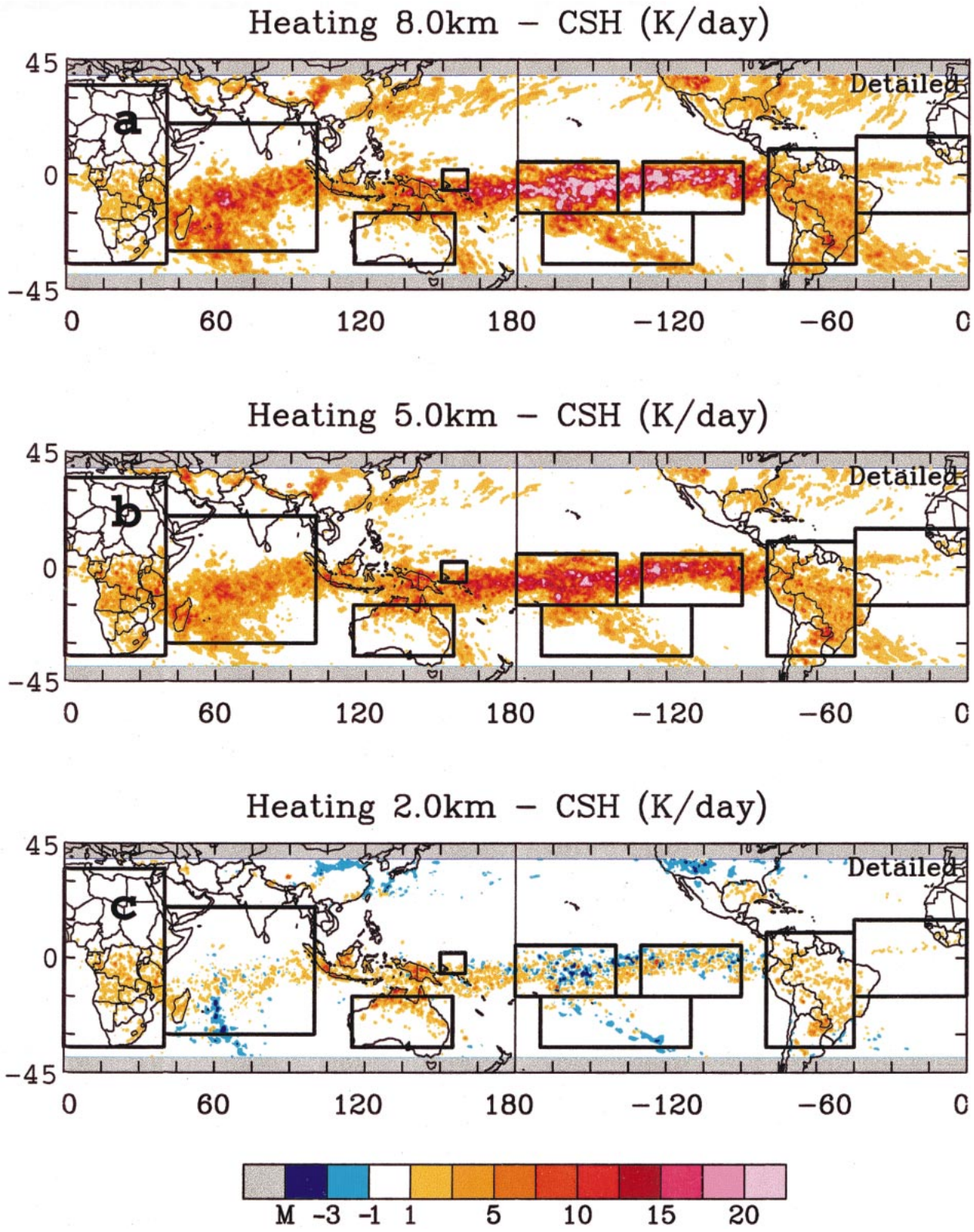

FIG. 6. Same as Fig. 5 except that latent heating profiles from the CSH lookup table representing the corresponding geographic locations were used. See text for more details.

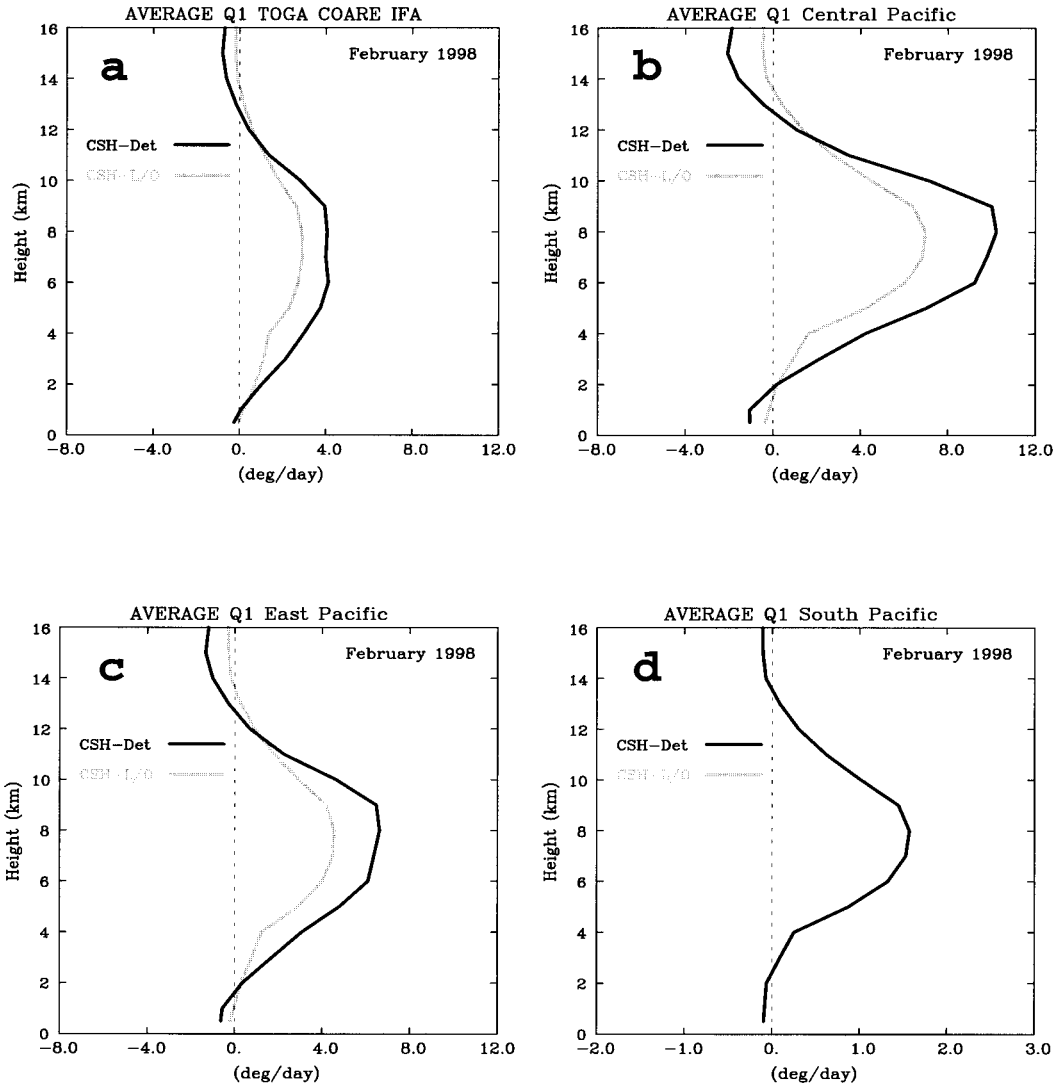

FIG. 7. Monthly (Feb 1998) mean latent heating profiles derived from the CSH heating algorithm for various geographic locations. Both approaches for selecting heating profiles from the lookup table (general land/ocean as in Fig. 5 or more detailed as in Fig. 6) are shown. The geographic areas are (a) the TOGA COARE IFA, (b) the central Pacific, (c) the east Pacific, (d) the South Pacific Convergence Zone, (e) the Indian Ocean, (f) the Atlantic Ocean (also shown using GCE GATE simulation profiles only), (g) South America, (h) Africa, and (i) Australia. Note that the abscissa scales for Figs. 7a–i are not always the same.

should be the subject of future studies using multiseason and multiyear retrieved latent heating profiles.

Comparison of latent heating profiles derived from the first and second approaches reveals stronger heating in the middle and upper troposphere and stronger cooling at low levels based upon the second approach over the central Pacific, east Pacific, and TOGA COARE IFA. On the other hand, relatively small differences in latent heating magnitudes are seen in other geographic locations. Over Africa and Australia, the maximum latent heating shifts to a lower level (about 5–6 km altitude) using the second approach. Conversely, the altitude of maximum latent heating is elevated, based upon the second approach, over the South American region. Over the Atlantic Ocean, a secondary maximum of latent heating is located at 3 km (with a primary maximum at middle levels) when the GCE model–simulated heating profiles are selected from the CSH-algorithm lookup table.

3) TEMPORAL VARIATION OF LATENT HEATING PROFILES

Time (daily) series of latent heating profiles derived from the CSH algorithm based upon the second approach (in selecting the latent heating profiles from the lookup table) for nine different geographic locations are shown in Fig. 8. The maximum latent heating level

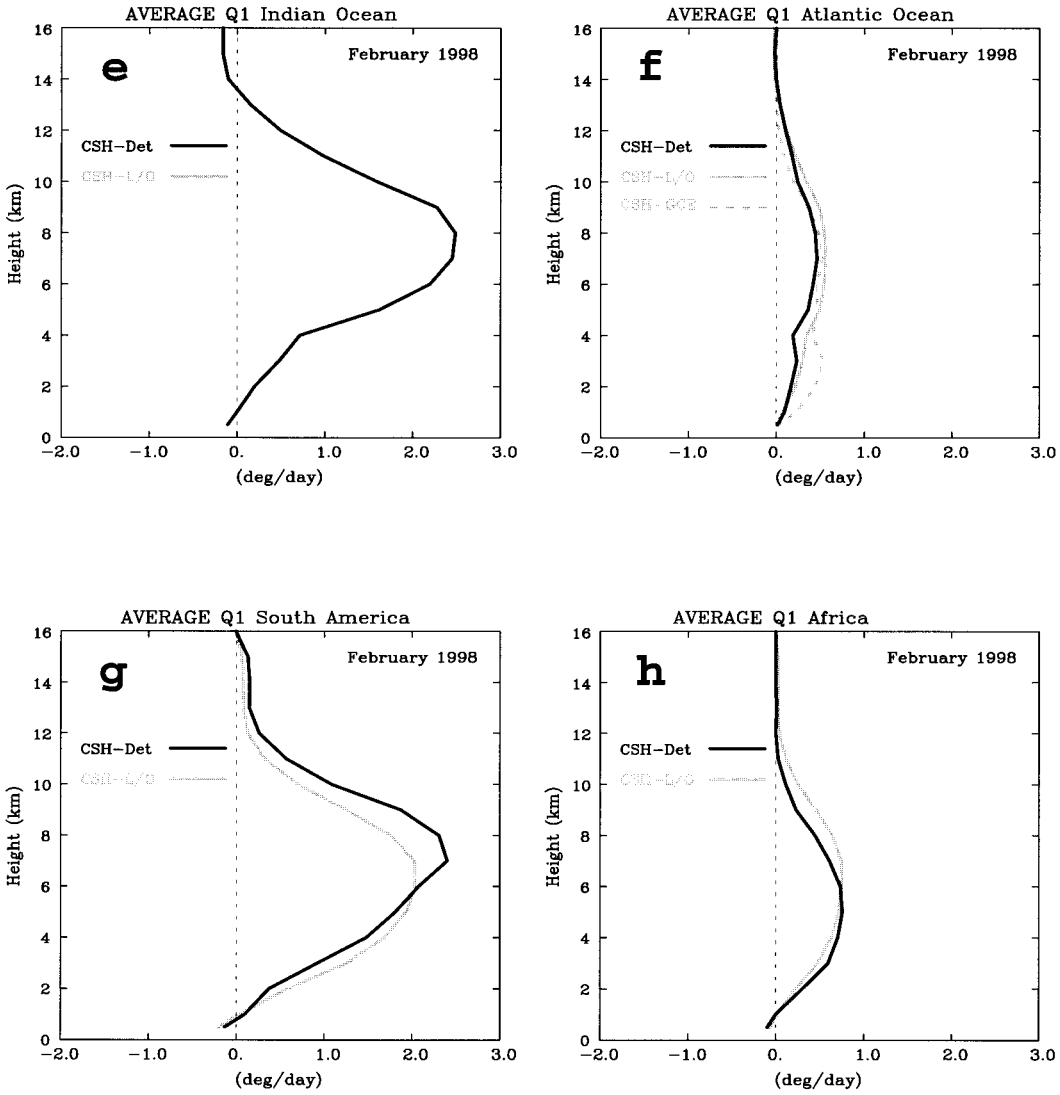

FIG. 7. (*Continued*)

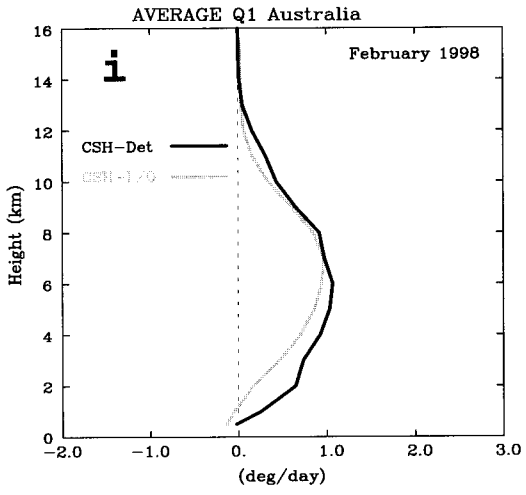

FIG. 7. (*Continued*)

varies with time for various convective events over Australia and the TOGA COARE IFA area. For latent heating profiles retrieved over the central, east, and South Pacific Ocean, the Indian Ocean, South America, and Africa, there is an almost constant maximum heating level, however. As discussed in Tao et al. (1993a), one of the major characteristics of the CSH algorithm is that the level of maximum latent heating is mainly determined by the stratiform percentage. This fact implies that there was no significant temporal (daily) variation in stratiform rainfall in the convective activity.

Frank et al. (1996) analyzed latent heating profiles for the 120 days (from 1 November 1992 to 28 February 1993) of the TOGA COARE intensive observation period using an enhanced network of rawinsonde stations. They examined the heating profiles over several arrays, including the IFA (about 7° × 5°), the outer sounding array (OSA; 15° × 15°) and the large-scale array (25°

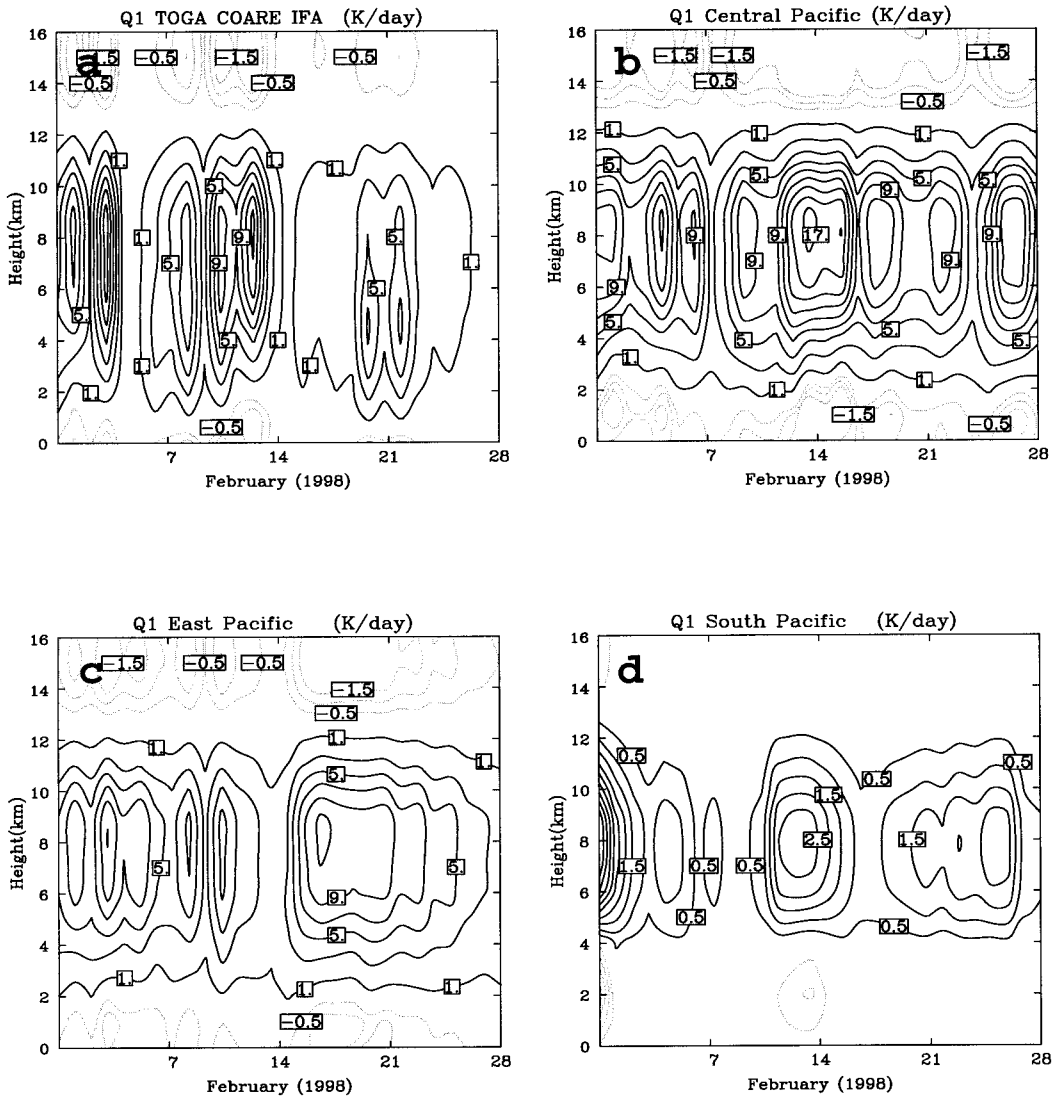

FIG. 8. Time (daily) series of latent heating profiles (K day^{-1}) derived from the CSH heating algorithm for various geographic locations. The geographic areas are (a) the TOGA COARE IFA, (b) the central Pacific, (c) the east Pacific, (d) the South Pacific Convergence Zone, (e) the Indian Ocean, (f) the Atlantic Ocean, (g) South America, (h) Africa, and (i) Australia. Note that the contour intervals are not always the same for (a)–(i).

$\times$ 30°). The results showed an interesting feature that was remarkably similar (i.e., maximum heating near 400 hPa, about 8 km above ground level) for all three arrays over 120 days. Lin and Johnson (1996) compared the mean latent heating from the IFA, OSA, and Marshall Islands region (Yanai et al. 1973). They also found that the heating profiles over the western Pacific, although from regions with distinctly different convective characteristics, are surprisingly similar to one another. The maximum heating also occurred near 400 hPa as indicated by Frank et al. (1996). The CSH algorithm–retrieved latent heating structures and their small temporal variation over the Pacific and the TOGA COARE IFA region are in good agreement with these diagnostic studies.

Over the TOGA COARE IFA, central and east Pacific (Figs. 8a,b,i), about six–eight convective events with life cycles from 2 to 3 days were identified. The temporal variation of the convective events retrieved over the SPCZ and Indian Ocean is smoother than that of the TOGA COARE IFA and the central and east Pacific. This result may imply that there are not just a few major convective events that dominate the total rainfall in these regions as compared with their counterparts over the TOGA COARE IFA and the central and east Pacific Ocean. The temporal variation of latent heating profiles over South America and Africa is not much different from that over adjacent oceans. This result may suggest that the temporal variability shows more of a geographic dependence than a land–ocean dependence. This sug-

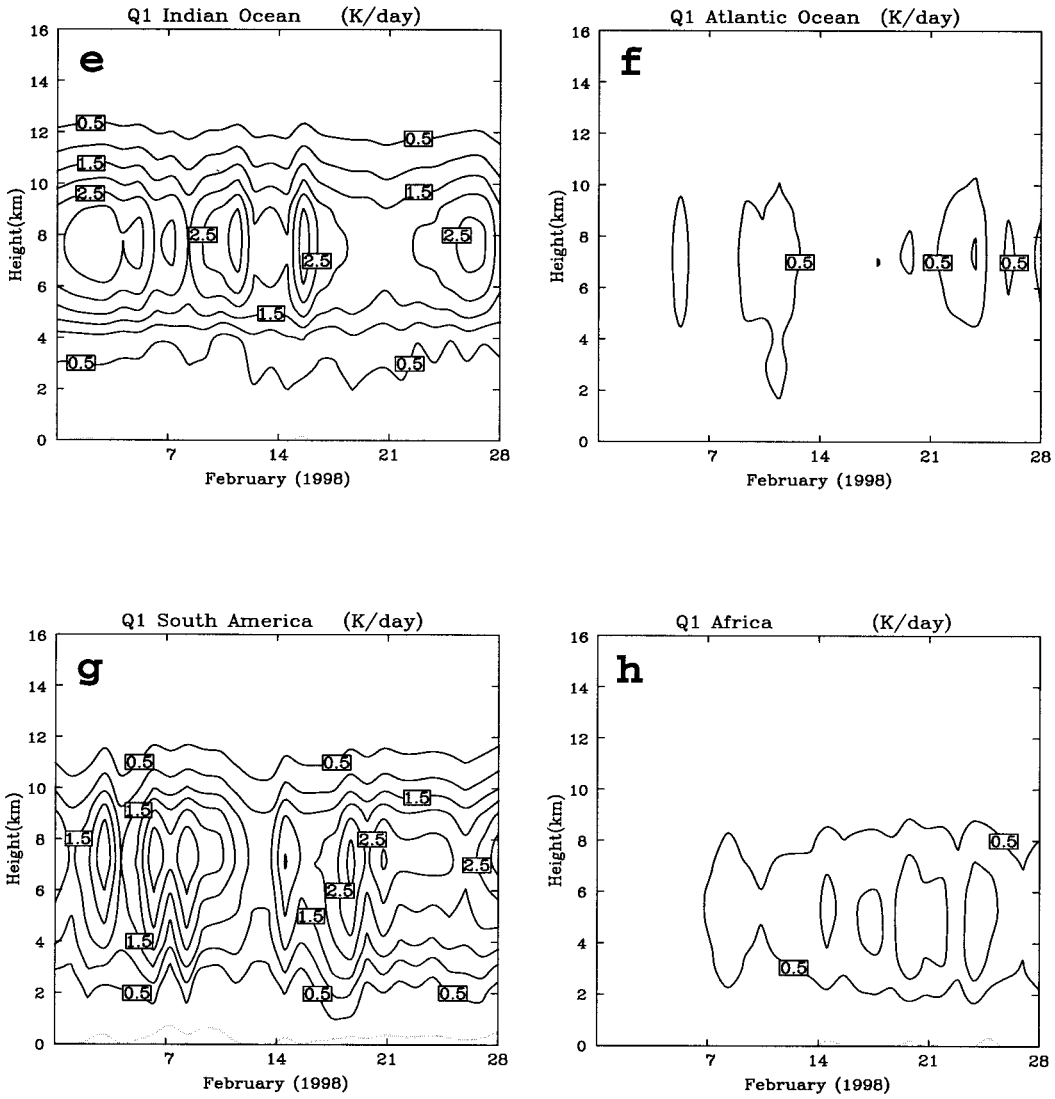

FIG. 8. (*Continued*)

gestion implies that cloud systems that develop over ocean can propagate (possibly through new generation) to adjacent land or vice versa. The above interpretations should be regarded with caution and may have major uncertainty because of the relatively poor sampling by the TMI. Other datasets (i.e., geostationary IR, global analyses, and the outgoing longwave radiation budget) are needed to scrutinize these interpretations. However, we note that there is good agreement regarding the number of major convective events over the TOGA COARE IFA region retrieved by the CSH algorithm for 1998 and diagnostically estimated for 1993. For example, the CSH algorithm–retrieved heating profiles indicate seven major convective events (maximum heating rate of over 6 K day^{-1}) over the IFA region. The diagnostic budget shown in Fig. 10d in Lin and Johnson (1996) has seven–eight major events (maximum heating rates over 3 K day^{-1}).

There are several notable differences between the CSH algorithm temporal latent heating variation and that deduced from diagnostic studies over the TOGA COARE region (Lin and Johnson 1996), GATE (Chen 1980), and AMEX (Frank and McBride 1989). First, there is no significant cooling between two adjacent convective events (diurnal variation), because the CSH algorithm is based on surface rainfall. If there is no surface rainfall (i.e., inactive convection or a suppressed period), the CSH algorithm will not produce any heating or cooling. Second, there is no temporal variation in heating or cooling in the lower troposphere as seen during TOGA COARE and GATE. The above two problems are, perhaps, the major shortcomings of the current CSH algorithm. Third, the AMEX convective systems show little variability over system lifetimes or from system to system based on budget studies. The CSH algorithm–estimated latent heating struc-

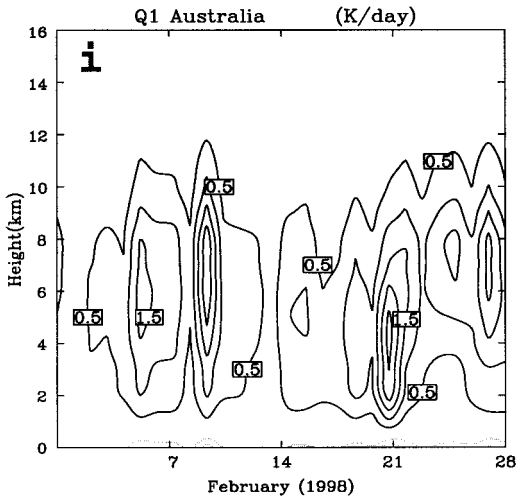

FIG. 8. (*Continued*)

ture over Australia (Fig. 8h) does show strong temporal variation (the maximum heating level changes from system to system).

5. Comparison of latent heating profiles derived by different heating retrieval algorithms

a. Horizontal distribution of latent heat release

Monthly mean latent heating profiles at three different altitudes (2, 5, and 8 km) using the GPROF heating algorithm over the Tropics are shown in Fig. 9. The global patterns of GPROF latent heating are similar to those derived from the CSH algorithm. However, there are several notable differences in the latent heating distributions from GPROF and the CSH algorithm. Strong cooling occurs from the low to middle troposphere from 25° to 35°N in the Pacific and Atlantic Oceans in the GPROF estimates. The areas of strong cooling in the lower troposphere in the central Pacific, east Pacific, and TOGA COARE IFA regions are very small. Most low-level cooling occurs over the SPCZ. Also, the heating at the 5-km level is as strong as the heating at the 8-km level over the central Pacific, east Pacific, and South America. This result implies that multiple maxima of heating could occur in these regions. These differences between the GPROF heating and the CSH algorithm–estimated latent heating structures are more than expected, because the GPROF heating algorithm uses mainly GCE model–simulated latent heating profiles in its supporting database; these heating profiles also represent the primary database for the CSH algorithm's lookup table. One possible difference is that the profiles stored in the CSH algorithm's lookup table represent a life cycle (typically over 2–4 h) of clouds/cloud systems. In the GPROF heating algorithm's database, the latent heating profiles represent the instantaneous latent heating corresponding to the hydrometeors that match the TMI observations.

Presented in Fig. 10 are the monthly mean latent heating profiles derived using the HH algorithm. The overall latent heating distributions estimated by the HH algorithm and the CSH algorithm are in good agreement with each other at the 5- and 8-km levels. The similarity between the GPROF heating algorithm– and HH algorithm–estimated latent heating between 30°S and 30°N in the middle and upper troposphere is remarkable. The multiple maxima of heating produced by the GPROF heating algorithm may also be present in the HH algorithm estimates over the central Pacific, the east Pacific, the Indian Ocean, and South America. One of the major differences between the HH algorithm's and the CSH and GPROF heating algorithms' estimated heating distributions is in the lower troposphere. The HH algorithm heating is much weaker over all three continental regions (Africa, Australia, and South America). The heating over the Pacific and Indian Oceans is also weak in comparison with the other two heating retrieval methods. Also note that there is no strong low-level cooling over the Pacific region as estimated by the other two methods. The HH-derived heating seen at low and middle levels from 30° to 35°N over the Pacific and Atlantic Oceans is not retrieved by either the CSH or the GPROF heating algorithms.

b. Monthly mean latent heating profiles over various geographic locations

The monthly (February 1998) averaged latent heating profiles derived from the three different heating retrieval algorithms[9] over various geographic locations are shown in Fig. 11. Also the CSH heating algorithm estimates using PR rainfall information are shown for comparison. The GPROF algorithm– and HH algorithm–estimated mean latent heating profiles over the TOGA COARE IFA, central Pacific, and east Pacific regions are in better agreement with each other than they are with the CSH algorithm estimates. The GPROF heating profiles exhibit a broad region of heating aloft with two embedded maxima (one near 4 km and another at near 6-km altitude). The double maxima are likely an artifact of the heating profile database that supplies the GPROF algorithm with candidate solutions. The HH algorithm–estimated heating profiles are almost constant between the 4- and 8-km levels. By contrast, only one maximum heating level (at 8 km) is estimated by the CSH algorithm. Diagnostic budget studies (Nitta 1972; Yanai et al. 1973; Thompson et al. 1979; Frank et al. 1996; Lin and Johnson 1996) all indicate a single heating maximum at 7–8 km altitude. Another difference between the vertical latent heating profiles from the CSH algorithm and the other two methods occurs in the 3 to 5-km layer. An interesting result is that the HH algorithm–estimated latent heating shows cooling at low levels

[9] The first approach of selecting the latent heating profiles from the CSH lookup table is used for comparison.

even through the area of stronger cooling is not shown in Fig. 9. This result implies that the HH algorithm–estimated cooling is weaker but covers a larger area in comparison with the other two methods. The rainfall estimated from the PR is smaller than that estimated from the TMI (Table 2), and this difference is the reason for the weaker latent heat release in the CSH algorithm–estimated heating using the PR-derived rainfall information. Similar stratiform amounts derived from both the PR and TMI lead to a single maximum of heating at 8 km in the CSH algorithm.

The CSH- and HH algorithm–estimated latent heating profiles at middle and upper levels are in very good agreement over the SPCZ and Indian Ocean. The GPROF algorithm–estimated latent heating profiles in these regions again show two embedded maxima, but the bulk of the heating is concentrated near 6 km. Overall, GPROF heating is concentrated at lower altitudes than the CSH and HH algorithm heating estimates. The lower tropospheric cooling determined by the GPROF heating algorithm is very strong in comparison with that estimated from the other two methods. The same difference occurs between the CSH algorithm and the other two methods' estimated latent heating profiles in the 2- to 3–5-km layer over these two oceanic regions and the Pacific region. The lack of diagnostic budget studies in the SPCZ and Indian Ocean makes it very difficult to evaluate the performance of the three heating algorithms, however.

The latent heating profiles estimated over the Atlantic Ocean by the three different heating algorithms are in very good agreement with each other above the 4-km level. Low-level cooling is indicated by both the GPROF and HH methods but not by the CSH method. A distinct, single midlevel (about 4–5 km) heating maximum is seen in the mean heating profile determined from a diagnostic budget study during GATE (Thompson et al. 1979). None of the three methods retrieves this feature. Frank (1978), however, diagnosed multiple heating peaks for GATE cloud clusters during various stages of their life cycle [shown in Fig. 9 in Johnson (1992)].

The HH algorithm–estimated latent heating profiles show two distinct heating maxima (near 4 and 6 km) in the South American, African, and Australian regions. The GPROF heating algorithm also yields two heating maxima at about 3 and 6 km (less pronounced than in the HH-derived profiles, though). The CSH algorithm yields only a single broad heating maximum near 7, 6, and 6.5 km, respectively, for Australia, Africa, and South America. A single maximum in heating was obtained in AMEX–Australia just above the freezing (500–600 hPa) level (Frank and McBride 1989) and in ABLE–South America at 5–6 km (Greco et al. 1994). The general magnitudes of heating rates estimated by the GPROF and the HH algorithms are also greater than those estimated by the CSH method over these three continental regions. Also, different altitudes of maximum heating are determined from the CSH algorithm using TMI and PR rainfall information. This difference is because the stratiform rain amounts derived from these two sensors are very different over the continental regions (Table 2).

Presented in Fig. 12 are profiles of the apparent heat source Q_1 normalized by the observed precipitation rate from several diagnostic budget studies; namely, the western Pacific region (Reed and Recker 1971; Nitta 1972; Yanai et al. 1973), Florida (Johnson 1976), the eastern Atlantic GATE region (Thompson et al. 1979), West Africa (Chong and Hauser 1990), the west Pacific warm pool (TOGA COARE IFA) region (Lin and Johnson 1996), and the Great Plains (Gallus and Johnson 1991). All of the profiles represent the composite heating resulting from a number of convective events at various stages of their life cycles. All of these profiles show only one maximum heating level (between 4 and 7 km). The maximum heating also varies from 4.5 K day^{-1} (1 cm $\text{day}^{-1})^{-1}$ (GATE) to almost 10 K day^{-1} (1 cm $\text{day}^{-1})^{-1}$ (West Africa). All of the estimated latent heating profile maxima from the three algorithms fall within the range of 4–8 K day^{-1} (1 cm $\text{day}^{-1})^{-1}$ (Figs. 7 and 11 and Table 2).

6. Summary and future work

This paper represents the first attempt at using TRMM rainfall information to estimate the latent heating structure over the global Tropics for February of 1998. Three different latent heating algorithms, the Goddard convective–stratiform heating algorithm, the Goddard profiling algorithm for heating, and the hydrometeor heating algorithm, that were previously developed for remote sensing applications (i.e., TRMM) are used and their results are compared. The latent heating profiles over six oceanic regions (TOGA COARE IFA, central Pacific, South Pacific Convergence Zone, east Pacific, Indian Ocean, and Atlantic Ocean) and three continental regions (South America, central Africa, and Australia) are estimated and studied. Verification of the retrieved global and regional latent heating profiles is not an easy task because of the lack of direct observations both temporally and spatially on the global and regional scales. The heating profiles obtained from the results of diagnostic studies over a broad range of geographic locations (e.g., Yanai et al. 1973; Johnson 1984, 1992; Thompson et al. 1979; Houze 1989; Frank and McBride 1989; Greco et al. 1994; Frank et al. 1996; Lin and Johnson 1996) are used to provide comparisons and indirect validation for the CSH algorithm–, the HH algorithm–, and the GPROF heating algorithm–estimated heating profiles.

Two different approaches for selecting the latent heating profiles in the CSH lookup table were used and tested. The first approach used normalized heating profiles representing oceanic and continental regions that were obtained by averaging profiles from the lookup

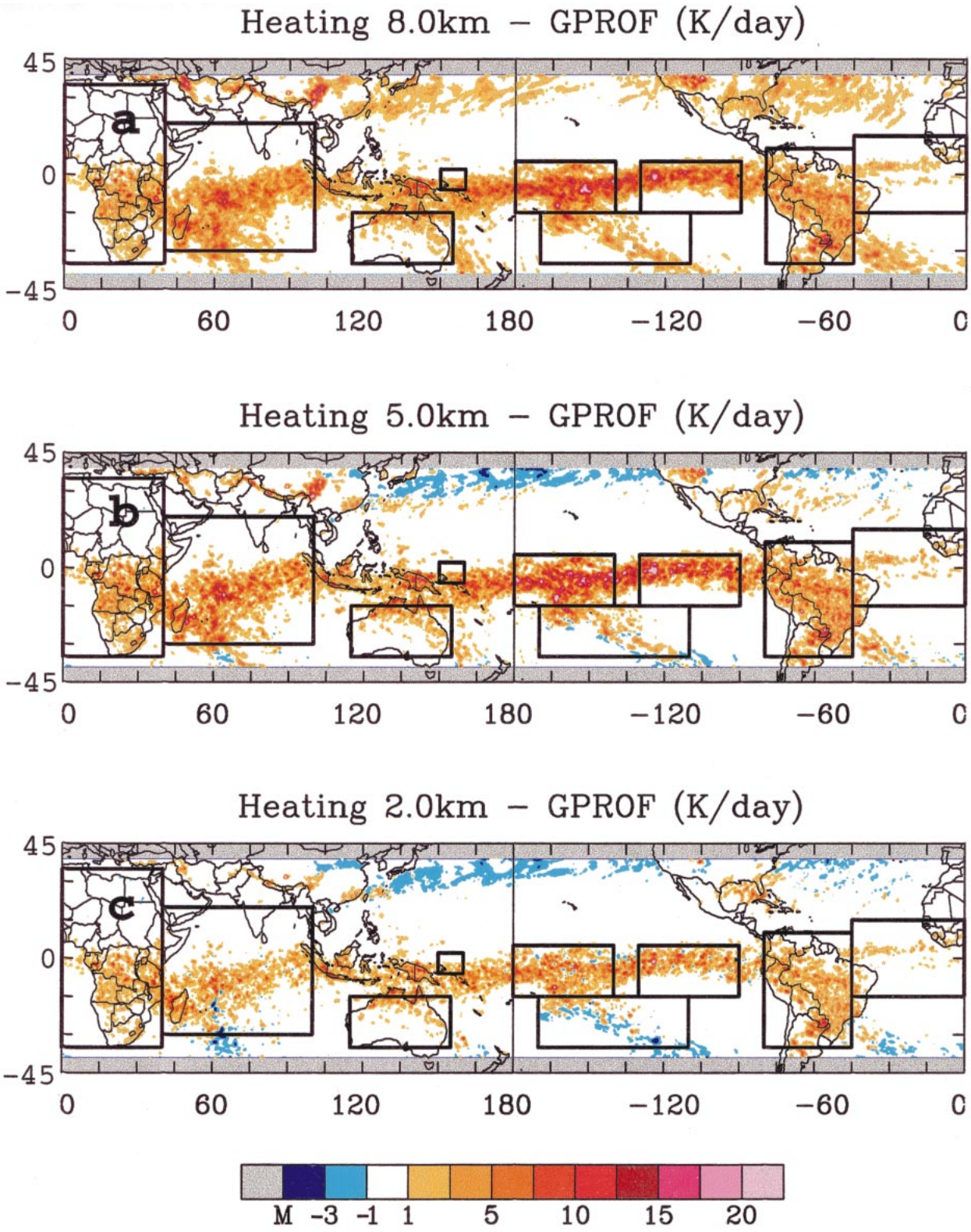

FIG. 9. Same as Fig. 5 but using the profile heating algorithm (Olson et al. 1999).

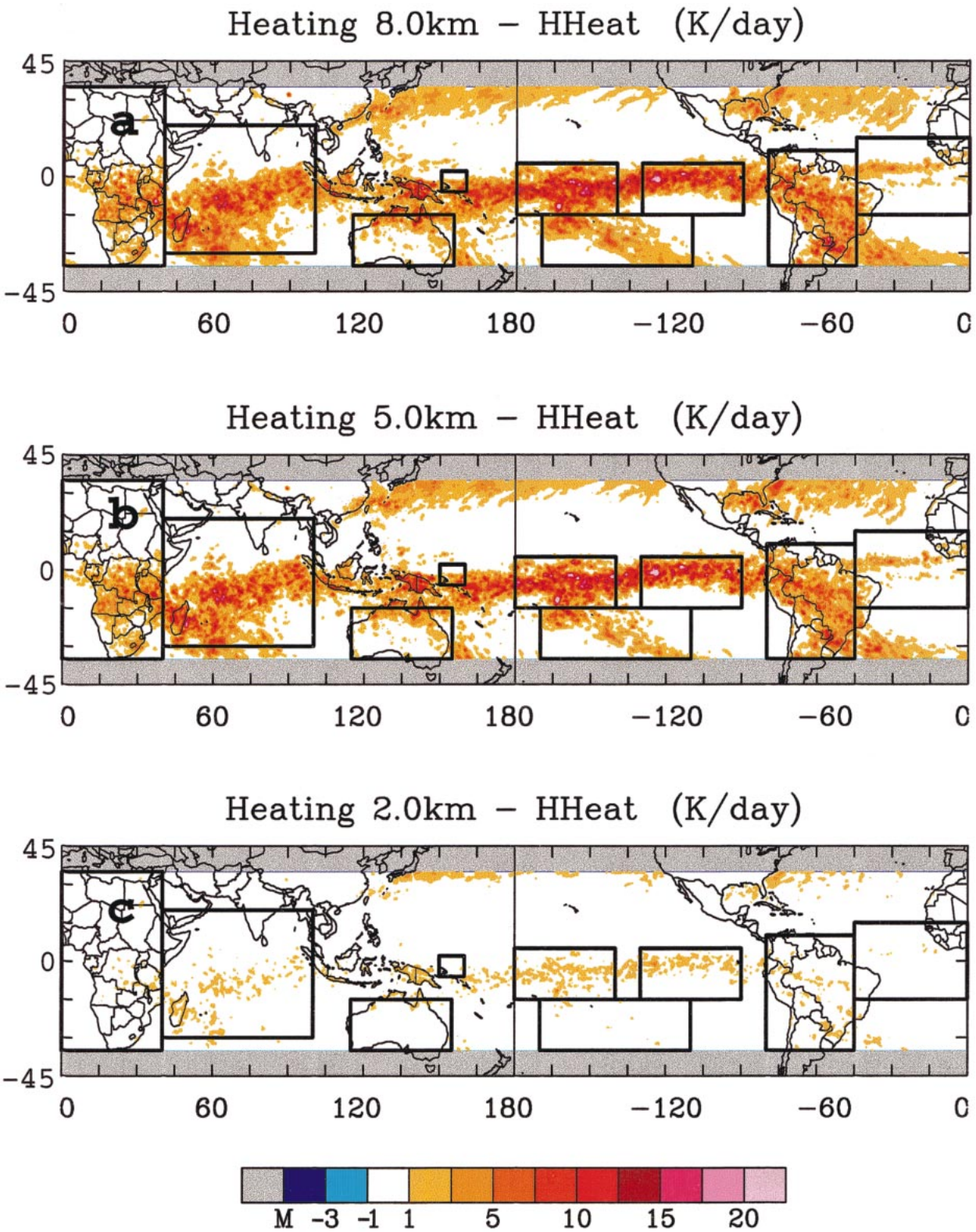

FIG. 10. Same as Fig. 5 but using the HH algorithm (Yang and Smith 1999a,b).

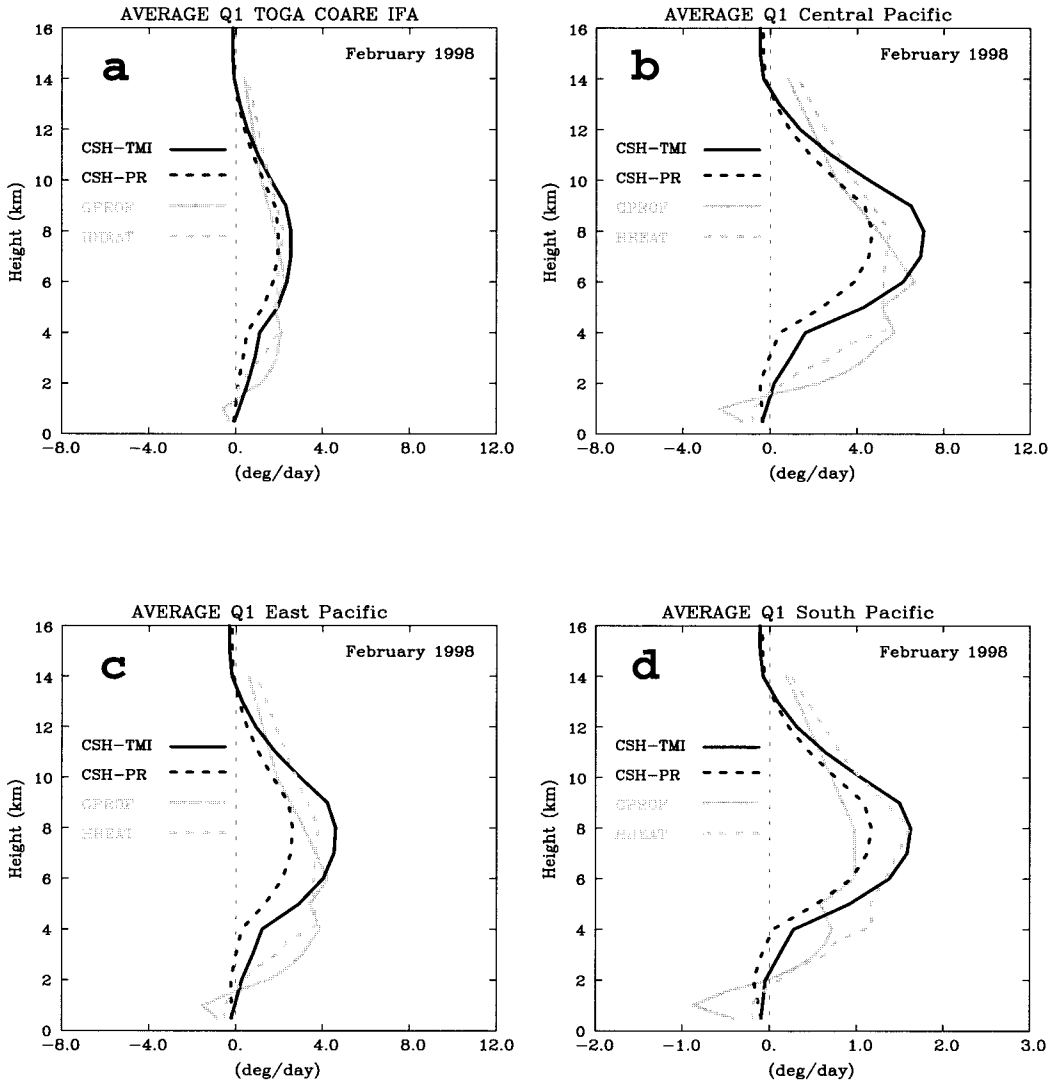

FIG. 11. Same as Fig. 7, but for a variety of retrieval methods (profile heating algorithm, HH algorithm, CSH using the PR rainfall product, and CSH using the TMI rainfall product).

table based on the growing (but still limited) set of GCE model simulations and diagnostic studies. In the second approach, the heating profiles from the lookup table are selected based on geographic locations and months of interest. The results showed that horizontal distributions and variations of latent heating structures (i.e., Pacific and Atlantic ITCZ, an SPCZ, and relatively scattered organization in Africa and South America) are not affected. Areas of cooling over the Pacific and Indian Oceans and heating over the continental regions at low levels are present in the retrieved latent heating structures using both approaches. Also, a single, broad maximum heating level in all geographic locations is produced by both approaches. However, there are some notable differences in terms of magnitude (1 K day^{-1} in the low troposphere to 2–3 K day^{-1} in the middle to upper troposphere) of the latent heat release and the altitude (by 1–2 km) of maximum heating. Finding a systematic method to select an appropriate set of profiles from the lookup table is an area that requires further investigation.

The rainfall estimated from the PR is less than that estimated from the TMI in the Pacific and Indian Oceans and the SPCZ, causing weaker latent heat release in the CSH algorithm estimated heating using the PR-derived rainfall information. Similar stratiform amounts derived from both the PR and TMI lead to a single maximum heating level at 8 km in the CSH algorithm over the tropical oceans. The larger stratiform amounts derived from the PR over South America and Australia consequently lead to higher maximum heating levels.

Table 3 summarizes the major characteristics of the latent heating profiles and structures estimated from the three different heating retrieval algorithms as well as

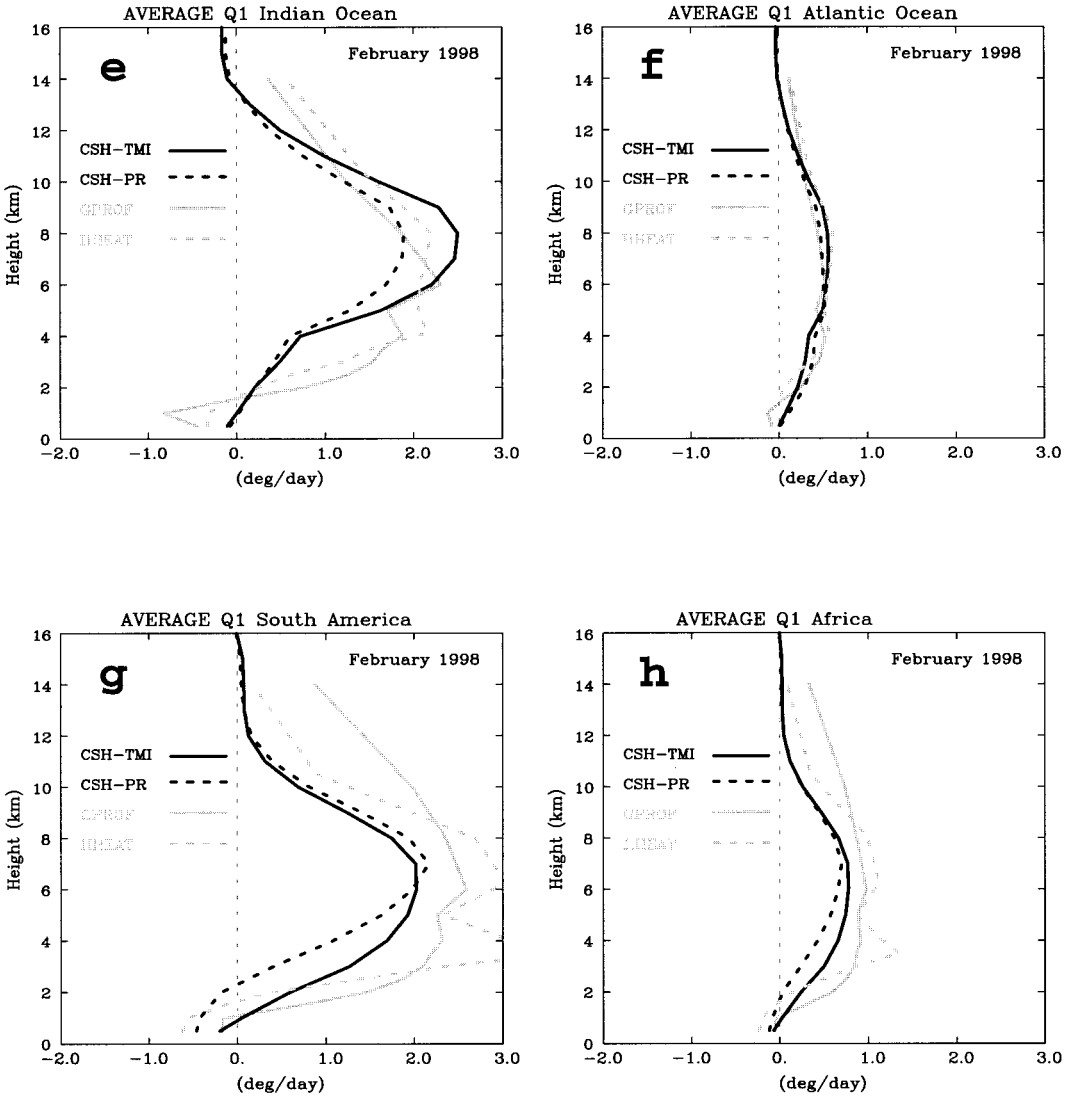

FIG. 11. (*Continued*)

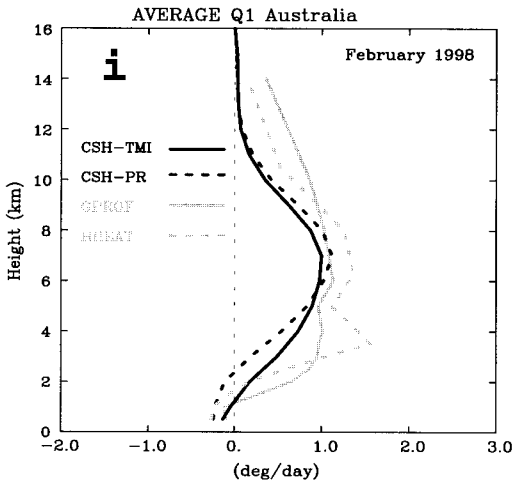

FIG. 11. (*Continued*)

previous diagnostic budget studies. The horizontal distributions or patterns of latent heat release from the three different heating retrieval methods are very similar. They can all identify the areas of major convective activity (i.e., a well-defined ITCZ in the Pacific, a distinct SPCZ) in the global Tropics. The magnitudes of their estimated latent heat release are in reasonable agreement. However, there are still some major differences among the CSH, GPROF, and HH algorithm-derived heating. For example, strong cooling in the low and middle troposphere is retrieved by the GPROF heating algorithm over the North Pacific Ocean. The feature is not retrieved by either the HH or CSH heating algorithms. Low-level cooling over Asia and the North American continent is retrieved by the CSH algorithm but not by the HH and GPROF algorithms. The HH heating algorithm does not retrieve areas of strong cooling over the oceans and heating over land at 2 km like

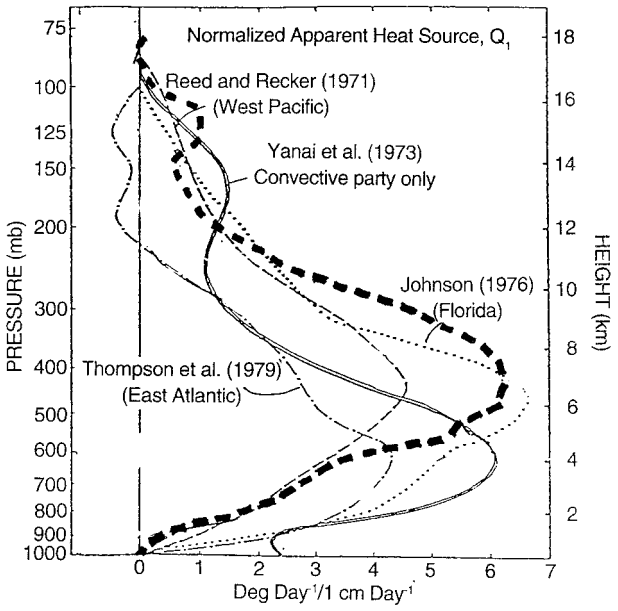

FIG. 12. Normalized Q_1 [(K day^{-1}) (cm day^{-1})$^{-1}$] for observations in the west Pacific, east Atlantic, and Florida regions. This figure was adapted from Johnson (1984). Normalized Q_1 profile averaged from three different TOGA COARE IFA convective periods 10–17 Dec 1992; 19–26 Dec 1992, and 9–13 Feb 1993) is also shown in the heavy dashed line. The TOGA COARE profile is provided by Lin and Johnson (1996).

the other heating algorithms do. Another major difference among these three retrieval algorithms is in the inferred altitude of the maximum heating. The CSH algorithm–estimated heating profiles show only one maximum heating level, and the level varies with convective activity from various geographic locations. In contrast, two embedded maxima within a broad layer of heating were found using the GPROF and HH algorithms, and the height variation of heating is less sensitive to variations in convective activity in different geographic locations. All algorithms concur that deep latent cooling does not occur during convective break periods. The diurnal variation of low-level latent heating structures seen in diagnostic budget studies during TOGA COARE cannot be retrieved because of the poor temporal sampling of TRMM.

It is important to note that the vertical heating structure derived from the CSH algorithm is largely determined by the surface rain rate and stratiform proportion. The vertically integrated heating is proportional to the surface rain rate, and the altitude of maximum heating increases with stratiform proportion.

Details of the vertical heating structure are determined by the cloud-resolving model profiles in the algorithm's lookup table. The heating profiles from GPROF should also be fairly consistent with the surface rain rate and stratiform proportion, given that the retrieved profiles are based upon cloud-resolving model simulations, but in this case additional information from the TMI radiance fields influences the retrieved profiles. There is a tendency for this algorithm to select heating profiles from one of the tropical squall line CRM simulations, which exhibits a relative minimum in heating at midlevels, and it therefore produces two peaks in heating. This kind of artifact will likely be eliminated as more cloud-resolving model simulations are added

TABLE 3. Major characteristics of latent heating profiles/structures estimated from three different heating retrieval algorithms and from previous diagnostic budget studies.

	CSH algorithm	GPROF heating algorithm	HH algorithm	Budget studies
Magnitude (maximum heating rates)	4–6* K day^{-1} (1 cm day^{-1})$^{-1}$	4–6 K day^{-1} (1 cm day^{-1})$^{-1}$	4–6 K day^{-1} (1 cm day^{-1})$^{-1}$	4–10 K day^{-1} (1 cm day^{-1})$^{-1}$
Horizontal variation	Similar patterns as surface rainfall (i.e., ITCZ over Pacific and an SPCZ). Relative strong low-level cooling over portion of Pacific Ocean.	Similar paterns as surface rainfall (i.e., ITCZ over Pacific and an SPCZ). Strong low–middle cooling from 25°–35° N in Pacific and Atlantic Oceans.	Similar patterns as surface rainfall (i.e., ITCZ over Pacific and an SPCZ). Area with weak low-level heating and cooling very large.	Inadequate observations.
Maximum heating level	Single max in all geographic locations. Higher (8-km level) in Pacific and Indian Oceans and SPCZ. Lower in Africa, Australia and South America.	Multiple peaks over most geographic locations except Africa. Its higher max is lower than the CSH estimated over Pacific, Indian Ocean, and TOGA COARE.	Multiple peaks over most geographic locations except SPCZ and Pacific Ocean. Its higher max is almost the same as the CSH estimated.	Single max in GATE, AMEX, TOGA COARE, ABLE, PRESTORM, and others. Higher in TOGA COARE. Lower in AMEX, GATE, and ABLE.
Notes	No temporal variation. No cooling between active convective events. No temporal variation in low levels (i.e., diurnal variation).	Altitude of max heating varies weakly with geographic locations. Strong cooling in mid-level over subtropics.	No areas showing strong heating over land and cooling over oceans at 2-km level.	Need more observations over various geographic locations in different seasons.

* 4–8 K day^{-1} (1 cm day^{-1})$^{-1}$ if different heating profiles are selected from lookup table.

to the algorithm's supporting database. Also, an effort is under way to prescribe better the radiative properties of hydrometeors in the GPROF algorithm based upon an examination of recent TRMM field campaign data. It is hoped that this effort will lead to a better interpretation of TMI radiances in the algorithm and to greater consistency between GPROF- and CSH-retrieved heating profiles. The HH algorithm relies upon the GPROF-retrieved vertical precipitation profiles as input and yields consistent heating profiles based upon hydrometeor conservation principles. It is not surprising, then, that the HH-retrieved heating profiles are somewhat similar to the GPROF heating profiles.

Heating profiles for the TRMM field campaign sites (i.e., the South China Sea Monsoon Experiment, May–June 1998; Large-Scale Biosphere–Atmosphere Experiment–TRMM–Brazil, January–February 1999; and the Kwajalein Experiment, July–September 1999) and other major field campaigns such as the U.S. Department of Energy Atmospheric Radiation Program will be produced using the three different heating algorithms, and these profiles will be compared with profiles determined from the field campaign sounding networks. This future comparison can provide an assessment of the absolute and relative errors of the heating retrieval algorithms. In addition, global analyses will be used to identify and to compare the large-scale circulation patterns for the retrieved periods and for periods during previous field campaigns (i.e., TOGA COARE and GATE). It is reasonable to assume that the latent heating structures for westerly wind bursts and super cloud clusters occurring in similar large-scale circulations and with similar SSTs may not be very different.

Four-dimensional fields of latent heating from The Florida State University (FSU) global model at the resolution T170 will also be compared (T. N. Krishnamurti 2000, personal communication). This comparison may provide information about the capabilities and deficiencies of the current moist processes represented in the FSU global model (as well as other GCMs and climate models). A regional (0.5°) daily four-dimensional latent heating structure can be produced over the lifetime of TRMM (November 1997 to the mission's end). The regional-scale products will be averaged to generate a 5° monthly latent heating profile product. Long-term latent heating structures are needed to improve our understanding of the interaction between the large-scale circulation and convectively generated latent heat release. In addition, the TRMM-estimated four-dimensional latent heating structures can be used as forcing in theoretical studies of the intraseasonal oscillation and its relationship/interaction with the onset of ENSO (Sui and Lau 1989).

Acknowledgments. This study is supported by the NASA Headquarters Physical Climate Program and by the NASA TRMM project. The authors are also grateful to Dr. R. Kakar (NASA/HQ) for his support of this research. We also thank three anonymous reviewers for their constructive comments that improved the clarity of the presentation in this paper. Acknowledgment is also made to the NASA Goddard Space Flight Center for computer time used in the research.

REFERENCES

Amayenc, P., J. P. Diguet, M. Marzoung, and T. Tani, 1996: A class of single- and dual-frequency algorithms for rain-rate profiling from a spaceborne radar. Part II: Tests from airborne radar measurements. *J. Atmos. Oceanic Technol.,* **13,** 142–164.

Awaka, J., T. Iguchi, and K. Okamoto, 1998: Early results on rain type classification by the Tropical Rainfall Measuring Mission (TRMM) precipitation radar. *Proc. Eighth URSI Commission F Open Symp.,* Aveiro, Portugal, URSI, 143–146.

Caniaux, G., J.-L. Redelsperger, and J.-P. Lafore, 1994: A numerical study of the stratiform region of a fast-moving squall line. Part I: General description and water and heat budgets. *J. Atmos. Sci.,* **51,** 2046–2074.

Chen, Y.-L., 1980: The relationship between organized convective systems and large-scale fields observed in GATE. Ph.D. thesis, University of Illinois, 148 pp. [Available from Dept. of Atmospheric Sciences, University of Illinois, 105 S. Gregory St., Urbana, IL 61801.]

Chong, M., and D. Hauser, 1990: A tropical squall line observed during the COPT 81 experiment in West Africa. Part III: Heat and moisture budgets. *Mon. Wea. Rev.,* **118,** 1696–1706.

Fitzjarrald, D. R., K. E. Moore, O. M. R. Cabral, J. Scala, A. O. Manzi, and L. D. de Abreu, 1990: Daytime turbulent exchange between the Amazon forest and the atmosphere. *J. Geophys. Res.,* **95,** 16 825–16 838.

Frank, W. M., 1978: The life cycles of GATE convective systems. *J. Atmos. Sci.,* **35,** 1256–1264.

——, and J. L. McBride, 1989: The vertical distribution of heating in AMEX and GATE cloud clusters. *J. Atmos. Sci.,* **46,** 3464–3478.

——, H. Wang, and J. L. McBride, 1996: Rawinsonde budget analysis during the TOGA COARE IOP. *J. Atmos. Sci.,* **53,** 1761–1780.

Gallus, W. A., Jr., and R. H. Johnson, 1991: Heat and moisture budgets of an intense midlatitude squall line. *J. Atmos. Sci.,* **48,** 122–146.

Greco, S., J. Scala, J. Halverson, H. L. Massie, W.-K. Tao, and M. Garstang, 1994: Amazon coastal squall lines. Part II: Heat and moisture transports. *Mon. Wea. Rev.*, **122,** 623–635.

Hitschfeld, W., and J. Bordan, 1954: Errors inherent in the radar measurement of rainfall at attenuating wavelengths. *J. Atmos. Sci.,* **11,** 58–67.

Hong, Y., C. D. Kummerow, and W. S. Olson, 1999: Separation of convective and stratiform precipitation using microwave brightness temperature. *J. Appl. Meteor.,* **38,** 1195–1213.

Houze, R. A., Jr., 1982: Cloud clusters and large-scale vertical motions in the Tropics. *J. Meteor. Soc. Japan,* **60,** 396–409.

——, 1989: Observed structure of mesoscale convective systems and implications for large-scale heating. *Quart. J. Roy. Meteor. Soc.,* **115,** 425–461.

——, 1997: Stratiform precipitation in regions of convection: A meteorological paradox. *Bull. Amer. Meteor. Soc.,* **78,** 2179–2196.

——, and E. N. Rappaport, 1984: Air motions and precipitation structure of an early summer squall line over the eastern tropical Atlantic. *J. Atmos. Sci.,* **41,** 553–574.

Huffman, G. J., and Coauthors, 1997: The Global Precipitation Climatology Project (GPCP) Combined Precipitation Dataset. *Bull. Amer. Meteor. Soc.,* **78,** 5–20.

Iguchi, T., and R. Meneghini, 1994: Intercomparisons of single-frequency methods for retrieving a vertical rain profile from airborne or spaceborne radar data. *J. Atmos. Oceanic Technol.,* **11,** 1507–1516.

——, Kozu, R. Meneghini, J. Awaka, and K. Okamoto, 1998: Pre-

liminary results of rain profiling with TRMM precipitation radar. *Proc. URSI-F Int. Triennial Open Symp. on Wave Propagation and Remote Sensing,* Aveiro, Portugal, URSI, 147–150.

——, ——, ——, ——, and ——, 2000: Rain profiling algorithm for the TRMM precipitation radar. *J. Appl. Meteor.*, **39,** 2038–2052.

Johnson, R. H., 1976: The role of convective-scale precipitation downdrafts in cumulus and synoptic scale interactions. *J. Atmos. Sci.,* **33,** 1890–1910.

——, 1984: Partitioning tropical heat and moisture budgets into cumulus and mesoscale components: Implication for cumulus parameterization. *Mon. Wea. Rev.,* **112,** 1656–1665.

——, 1992: Heat and moisture sources and sinks of Asian monsoon precipitating systems. *J. Meteor. Soc. Japan,* **70,** 353–371.

——, and P. J. Hamilton, 1988: The relationship of surface pressure features to the precipitation and airflow structure of an intense midlatitude squall lline. *Mon. Wea. Rev.,* **116,** 1444–1471.

——, and P. E. Ciesielski, 2000: Rainfall and radiative heating estimates from TOGA COARE atmospheric budgets. *J. Atmos. Sci.,* **57,** 1497–1514.

Kummerow, C., W. S. Olson, and L. Giglio, 1996: A simplified scheme for obtaining precipitation and vertical hydrometeor profiles from passive microwave sensors. *IEEE Trans. Geosci. Remote Sens.,* **34,** 1213–1232.

Liao, L., R. Meneghini, and T. Iguchi, 1999: Simulations of mirror image return of air/space-borne radar in rain and their applications in estimating path attenuation. *IEEE Trans. Geosci. Remote Sens.,* **37,** 1107–1121.

Lin, X., and R. H. Johnson, 1996: Heating, moistening and rainfall over the western Pacific during TOGA COARE. *J. Atmos. Sci.,* **53,** 3367–3383.

McCumber, M., W.-K. Tao, J. Simpson, R. Penc, and S.-T. Soong, 1991: Comparison of ice-phase microphysical parameterization schemes using numerical simulations of tropical convection. *J. Appl. Meteor.,* **30,** 985–1004.

Meneghini, R., J. Eckerman, and D. Atlas, 1983: Determination of rain rate from a spaceborne radar using measurements of total attenuation. *IEEE Trans. Geosci. Remote Sens.,* **21,** 34–43.

——, T. Iguchi, T. Kozu, L. Liao, K. Okamoto, J. A. Jones, and J. Kwiatkowski, 2000: Use of the surface reference technique for path attenuation estimates from TRMM precipitation radar. *J. Appl. Meteor.,* **39,** 2053–2070.

Nitta, T., 1972: Energy budget of wave disturbances over the Marshall Islands during the years of 1956 and 1958. *J. Meteor. Soc. Japan,* **50,** 71–84.

Olson, W. S., C. D. Kummerow, G. M. Heymsfield, and L. Giglio, 1996: A method for combined passive–active microwave retrievals of cloud and precipitation profiles. *J. Appl. Meteor.,* **35,** 1763–1789.

——, ——, Y. Hong, and W.-K. Tao, 1999: Atmospheric latent heating distributions in the Tropics derived from passive microwave radiometer measurements. *J. Appl. Meteor.,* **38,** 633–644.

Reed, R. J., and E. E. Recker, 1971: Structure and properties of synoptic-scale wave disturbances in the equatorial western Pacific. *J. Atmos. Sci.,* **28,** 1117–1133.

Rodgers, E. B., S. W. Chang, and H. F. Pierce, 1994: A satellite observational and numerical study of the precipitation characteristics in western North Atlantic tropical cyclones. *J. Appl. Meteor.,* **33,** 129–139.

Rutledge, S. A., and R. A. Houze Jr., 1987: A diagnostic modeling study of the trailing stratiform rain of a midlatitude squall line. *J. Atmos. Sci.,* **44,** 2640–2656.

Scala, J., and Coauthors, 1990: Cloud draft structure and trace gas transport. *J. Geophys. Res.,* **95,** 17 015–17 030.

Short, D. A., B. S. Ferrier, J. C. Gerlach, S. A. Rutledge, and O. W. Thiele, 1997: Shipboard radar rainfall patterns within the TOGA COARE IFA. *Bull. Amer. Meteor. Soc.,* **78,** 2817–2836.

Simpson, J., R. F. Adler, and G. R. North, 1988: A proposed satellite Tropical Rainfall Measuring Mission (TRMM). *Bull. Amer. Meteor. Soc.,* **69,** 278–295.

——, C. Kummerow, W.-K. Tao, and R. Adler, 1996: On the Tropical Rainfall Measuring Mission (TRMM). *Meteor. Atmos. Phys.,* **60,** 19–36.

Smith, E. A., X. Xiang, A. Mugnai, and G. J. Tripoli, 1992: A cloud-radiation model algorithm for spaceborne precipitation retrieval. Extended Abstract Volume, *Int. TRMM Workshop on the Processing and Utilization of the Rainfall Data Measured from Space, Tokyo, Japan,* Communications Research Laboratory, 273–283.

——, ——, ——, and ——,1994: Design of an inversion-based precipitation profile retrieval algorithm using an explicit cloud model for initial guess microphysics. *Meteor. Atmos. Phys.,* **54,** 53–78.

Steiner, M. R., R. A. Houze Jr., and S. E. Yuter, 1995: Climatological characterization of three-dimensional storm structure from operational radar and rain gauge data. *J. Appl. Meteor.,* **34,** 1978–2007.

Sui, C.-H., and K.-M. Lau, 1989: Origin of low-frequency (intraseasonal) oscillations in the tropical atmosphere. Part II: Structure and propagation of mobile wave-CISK modes and their modification by lower boundary forcings. *J. Atmos. Sci.,* **46,** 37–56.

Tao, W.-K., and J. Simpson, 1989: Modeling study of a tropical squall-type convective line. *J. Atmos. Sci.,* **46,** 177–202.

——, ——, S. Lang, M. McCumber, R. Adler, and R. Penc, 1990: An algorithm to estimate the heating budget from vertical hydrometeor profiles. *J. Appl. Meteor.,* **29,** 1232–1244.

——, ——, and S.-T. Soong, 1991: Numerical simulation of a subtropical squall line over the Taiwan Strait. *Mon. Wea. Rev.,* **119,** 2699–2723.

——, S. Lang, J. Simpson, and R. Adler, 1993a: Retrieval algorithms for estimating the vertical profiles of latent heat release: Their applications for TRMM. *J. Meteor. Soc. Japan,* **71,** 685–700.

——, J. Simpson, C.-H. Sui, B. Ferrier, S. Lang, J. Scala, M.-D. Chou, and K. Pickering, 1993b: Heating, moisture and water budgets of tropical and midlatitude squall lines: Comparisons and sensitivity to longwave radiation. *J. Atmos. Sci.,* **50,** 673–690.

——, and Coauthors, 2000: Vertical profiles of latent heat release and their retrieval in TOGA COARE convective systems using a cloud resolving model, SSM/I and radar data. *J. Meteor. Soc. Japan,* **78,** 333–355.

Thompson, R. M., Jr., S. W. Payne, E. E. Recker, and R. J. Reed, 1979: Structure and properties of synoptic-scale wave disturbances in the intertropical convergence zone of the eastern Atlantic. *J. Atmos. Sci.,* **36,** 53–72.

Yanai, M., S. Esbensen, and J. Chu, 1973: Determination of average bulk properties of tropical cloud clusters from large-scale heat and moisture budgets. *J. Atmos. Sci.,* **30,** 611–627.

Yang, S., and E. A. Smith, 1999a: Moisture budget analysis of TOGA COARE area using SSM/I retrieved latent heating and large scale Q_2 estimates. *J. Atmos. Oceanic Technol.,* **16,** 633–655.

——, and ——, 1999b: Four-dimensional structure of monthly latent heating derived from SSM/I satellite measurements. *J. Climate,* **12,** 1016–1037.

——, and ——, 2000: Vertical structure and transient behavior of convective–stratiform heating in TOGA COARE from combined satellite–sounding analysis. *J. Appl. Meteor.,* **39,** 1491–1513.